MEASURING THE ELECTRIC FIELD OF PICOSECOND TO NANOSECOND PULSES WITH HIGH SPECTRAL RESOLUTION AND HIGH TEMPORAL RESOLUTION

A Thesis
Presented to
The Academic Faculty

by

Jacob Cohen

In Partial Fulfillment
of the Requirements for the Degree
Doctor of Philosophy in the
School of Physics

Georgia Institute of Technology
December 2010

MEASURING THE ELECTRIC FIELD OF PICOSECOND TO NANOSECOND PULSES WITH HIGH SPECTRAL RESOLUTION AND HIGH TEMPORAL RESOLUTION

Approved by:

Dr. Rick Trebino, Advisor
School of Physics
Georgia Institute of Technology

Dr. Zhigang Jiang
School of Physics
Georgia Institute of Technology

Dr. Jennifer Curtis
School of Physics
Georgia Institute of Technology

Dr. Ken Brown
School of Physics
Georgia Institute of Technology

Dr. John Buck
School of Electrical Engineering
Georgia Institute of Technology

To my mother, Margaret Cohen, and father, Ronald Cohen.

ACKNOWLEDGEMENTS

I wish to thank first my parents, because without their support I would not be here. Next, I would like to thank all the people I have worked with including Pam, Peter, Vikrant, Rick, Pablo, Dongjoo, Chris, and Lina. I would particularly like to thank Pam for her help and effort answering my questions and especially helping with solutions to programming and experimental problems, like single-shot MUD TADPOLE, multi-shot MUD TADPOLE, and optimizing the filtering routine from hours to seconds. I also thank Vikrant for his help with understanding ultrafast concepts even late into the evenings in the lab, and for his GRENOUILLE idea. Additionally, I thank Peter for his expertise in nonlinear optics and helping in the design of the GRENOUILLE crystal. Next, I thank Rick for his constant support and willingness to help solve experimental problems at group meetings and over email. And, I thank Dongjoo for his help using and designing GRENOUILLEs. Lastly, I thank Linda and Samantha King for their help with administrative matters.

TABLE OF CONTENTS

LIST OF TABLES

LIST OF FIGURES

LIST OF SYMBOLS AND ABBREVIATIONS

TBP	Time-bandwidth product
SI	Spectral interferometry
SEA TADPOLE	Spatial encoded arrangement for temporal analysis by dispersing a pair of light E-fields
MUD TADPOLE	Multiple-delay for temporal analysis by dispersing a pair of light E-fields
FTSI	Fourier transform spectral interferometry
GVM	Group velocity mismatch
GVD	Group velocity dispersion
GRENOUILLE	Grating eliminated no-nonsense observation of ultrafast laser light E-fields
FROG	Frequency-resolved optical gating
CW	Continuous wave
fs	Femtosecond
ps	Picosecond
ns	Nanosecond
as	Attosecond
PFT	Pulse-front tilt
CPA	Chirped pulse amplification
OAWG	Optical arbitrary waveform generation

SUMMARY

The subject matter of this thesis is in the field of ultrashort pulse measurement. The succeeding chapters detail four new techniques for measuring the electric field of complex pulses with high temporal resolution *and* high spectral resolution.

First, we demonstrate an extremely simple frequency-resolved-optical gating (GRENOUILLE) device for measuring the intensity and phase of relatively long—ps—pulses. In order to achieve the required high spectral resolution and large temporal range, it uses a few-cm-thick second harmonic-generation crystal in the shape of a pentagon. This has the additional advantage of reducing the device's total number of components to as few as three simple easily aligned optics, making it the simplest device ever developed for complete pulse measurement. We report complete intensity-and-phase measurements of pulses up to 15ps long with a time-bandwidth product of 21.

Secondly, we introduce a variation of spectral interferometry (SI) using a virtually imaged phased array and grating spectrometer for measuring long complex ultrashort pulses up to 80 ps in length. To our knowledge this is the longest pulse every measured using Fourier transform SI (FTSI), and the first use of a VIPA/grating spectrometer for FTSI.

Next, we introduce a SI technique for measuring the complete intensity and phase of relatively long and very complex ultrashort pulses. Ordinarily, such a method would require a high-resolution spectrometer, but our method overcomes this need. It involves making multiple measurements using SI (in its SEA TADPOLE variation) at numerous delays, measuring many temporal pulselets within the pulse, and concatenating the resulting pulselets. Its spectral resolution is the inverse delay range—many times higher

than that of the spectrometer used. The waveforms were measured with ~40 fs temporal resolution over a temporal range of ~3.5ns and had time-bandwidth products exceeding 65,000, which to our knowledge is the largest time-bandwidth product ever measured with ~fs temporal resolution.

Finally, we demonstrate the first single-shot measurement technique that temporally interleaves hundreds of measurements with ~125 fs temporal resolution. It is another variation of SI for measuring the complete intensity and phase of relatively long and complex ultrashort pulses in a single shot. Ordinarily, such a method would require a high-resolution spectrometer, but by temporally interleaving many delayed spectral measurements our method overcomes this need. It uses a grating to introduce a transverse time delay into the reference pulse by tilting the pulse front. The tilted reference pulse is used to gate the unknown pulse by interfering it at the image plane of an imaging spectrometer. Our simple proof-of-principle implementation resulted in an increase in the spectral resolution of the spectrometer used by a factor of 15. It provided ~125 fs temporal resolution and a temporal range of 70 ps using a low-resolution spectrometer.

CHAPTER 1

AN INTRODUCTION TO MEASURING COMPLEX ULTRASHORT PULSES

1.1 Measuring ultrashort pulses, a solved problem?

The measurement of ultrashort pulses has been an evolving field of research for over 50 years. The research has been fruitful, so fruitful in fact, that ultrashort pulses in the range of a few fs to several ps are arguably the most well characterized of all laser sources. Counterintuitively, ultrashort pulsed lasers are better characterized than ns pulses, due to the high spectral resolution required for an accurate measurement of these longer events.

Yet, the advances in ultrafast metrology came gradually. The first measurement technique used to measure ultrashort pulses was autocorrelation. The autocorrelation technique was the early researchers answer to the ancient ultrafast metrology conundrum, "Since ultrashort pulses are the shortest events ever created, what should they use to measure them?" The answer was, use the event itself.

An autocorrelation measurement involves combining two replicas of the pulse in a nonlinear-optical crystal and scanning their relative delay in time. Although simple in design, it provides only a rough measure of the pulse length. Additionally, autocorrelators have other deficiencies. They require extremely thin crystals, which are difficult to manufacture. And, their experimental setup involves three very sensitive degrees of freedom, most temporal structure is smeared out in the retrieved intensity vs. time, and they yield no information about the phase (color) vs. time.

In 1991, Dan Kane and Rick Trebino introduced Frequency-Resolved Optical Gating (FROG) [1], which is simply a frequency-resolved autocorrelation. FROG

measures the complete intensity and phase vs. time and so solves the last two of these problems. As a result, FROG has become the gold standard for pulse measurement. Indeed, FROG and its many variations [1] have been used to measure pulses from ~100as [2] up to several ns.

Additionally, there are a number of other methods for measuring ultrashort pulses including spectral phase interferometry for direct electric field reconstruction (SPIDER) [3], which involves spectrally shearing a pulse and interfering it with an unsheared replica of itself at a spectrometer. However, the shortest pulse SPIDER can measure is limited by its stringent alignment issues [4], which are less problematic for longer pulses but remain severe.

Another technique commonly used to measure ultrashort pulses is spectral interferometry (SI) [5]. SI is conceptually very simple: it involves measuring the spectrum of the sum of a known reference pulse and an unknown pulse, the pulse under measurement. The pulses are delayed in time resulting in an interferogram at the spectrometer. Using a simple Fourier transform retrieval algorithm both the intensity and the phase difference of the unknown pulse can be retrieved. Additionally, if the spectral phase of the reference pulse is known, the full electric field of the unknown pulse can be retrieved.

As a result of these and other methods, characterizing ultrashort pulses from fs up to several ps is now routine. Consequently, pulse measurement scientists must look to other regimes in order to ply their trade.

1.2 Measuring complex ultrashort pulses and optical arbitrary waveform generation

The new frontier of pulse measurement is long pulses. The development of techniques for measuring longer pulses from many ps to 1 ns (even simple ones) has lagged far behind those for measuring shorter fs pulses. This is because many-ps pulses are still too short to be well resolved in time, and, from the classical uncertainty principle, such relatively long pulses can have narrow spectral features, which also can be difficult to resolve. A pulse with a temporal length of Δt exhibits spectral features $\delta\omega \sim 1/\Delta t$ wide, which must be resolved for its measurement. The complete measurement of fs near-IR pulses requires an easily attained spectral resolution of only ~1 nm. But any frequency- or time-frequency-domain measurement of, say, a 100 ps, 800 nm pulse requires a difficult-to-attain spectral resolution of < 0.01 nm. If the pulse also has 100 fs temporal structure, then, by a similar uncertainty-principle argument, it simultaneously requires a spectral *range* of > 10 nm—a difficult combination of capabilities.

Similar to fs metrology in which the driver has been the development of shorter and shorter pulses, the driving process in the complex pulse regime is the generation of more complex pulses or optical arbitrary waveforms. Optical arbitrary waveform generation (OAWG) [6] is the process in which the amplitude and phase of individual spectral modes of a frequency comb are modified. Indeed, progress in this field has driven optical metrology to develop new high temporal and spectral resolution techniques to measure transient optical waveforms [7-13]. Yet, even with these advances, no technique currently exists that has the necessary sub-100fs temporal resolution and ~10

ns temporal range, a value of 100,000 time-bandwidth product (TBP), to accurately characterize arbitrary waveforms.

One technique commonly used to measure pulses with large TBPs is cross-correlation frequency-resolved optical gating, XFROG [14-15]. Operating in the time-frequency domain, XFROG, in principle, must satisfy all four of the above conditions but, in practice, actually achieves temporal and spectral super-resolution by using one domain's slow variations to fill in the other's fast variation. As a result, it has measured complex continuum pulses with TBPs as high as ~5000. But retrievals of such complex pulses can take more than an hour on a standard desktop personal computer, and the massive data sets involved due to the two-dimensional nature of XFROG traces makes it difficult to imagine measuring significantly more complex pulses using it.

Several time-domain techniques based upon temporal imaging can measure the temporal intensity of subnanosecond pulses [11-12] by stretching them to ns in length. Additionally, streak cameras are often used to characterize pulses with ps temporal resolution. Yet, these techniques do not directly measure the phase of the pulse.

In an effort to increase the sensitivity, a number of linear techniques have been introduced. Indeed, several self-referenced linear interferometric techniques have been used to measure pulses up to 100ps long [16]. However, all these techniques require precise electrical synchronization of the pulse under test with the temporal modulator which limit the complexity of the pulse that can be measured.

Furthermore, SI can also be used to measure complex pulses. Although SI is very sensitive and has measured trains of zeptojoule-energy pulses [17], its most common implementation, Fourier Transform SI (FTSI) [5], lacks the spectral resolution to

characterize complex pulses [18]. Additionally, there have been numerous adaptations that improve upon the spectral resolution of SI [8-9, 19], yet even with these improvements, the spectral resolution of these variants is limited by that of the spectrometer used and the linear spectral trace.

As a result, pulses in the ps to ns regime are still not well characterized. Unlike the fs to few ps regime, no measurement technique has the required high temporal resolution and high spectral resolution to accurately resolve these longer pulses. In this thesis we introduce four new techniques for measuring complex pulses in this regime. Although none of these techniques solve the problem conclusively, we believe that the long temporal range, or equivalently the high spectral resolution, of each technique provides a substantial improvement to the field of optical arbitrary waveform metrology. Indeed, one of the techniques we introduce here actually has the necessary temporal resolution and spectral resolution to accurately characterize an optical arbitrary waveform (TBP = 100,000), yet it is multi-shot and therefore not applicable to transient optical phenomena.

1.3 Thesis outline

This thesis describes four simple experimental techniques that have been developed to measure the amplitude and phase of complex ultrashort pulses.

Chapter 2 describes an extension of the GRENOUILLE [20] technique to measure pulses between 200fs - 20ps in duration.

Chapter 3 introduces an extension to SI which uses a virtually imaged phased array (VIPA) spectrometer to increase the spectral resolution of SI and thereby measure pulses up to ~80ps in length.

Chapter 4 introduces an extension of SI called MUD TADPOLE specifically intended for measuring very long and complex pulses.

Chapter 5 details a MUD TADPOLE measurement of a pulse with a TBP of 65,000 and explains MUD TADPOLE's limits with regard to complex pulse measurement.

Chapter 6 introduces a single-shot MUD TADPOLE technique for measuring complex pulses which employs a reference pulse with the spatio-temporal distortion pulse-front tilt (PFT) to increase the spectral resolution of the device.

CHAPTER 2

HIGHLY SIMPLIFIED DEVICE FOR MEASURING PICOSECOND PULSES

Portions of this work appear in [21], J. Cohen, D. Lee, V. Chauhan, P. Vaughan, and R. Trebino, "Highly simplified device for measuring the intensity and phase of picosecond pulses," Opt. Express 18, 17484-17497 (2010).

2.1 Introduction

In this chapter, we introduce an extremely simple FROG capable of measuring pulses up to 15ps in length. As a FROG technique, it is complete, yielding the intensity and phase vs. time and frequency with only easily removed, trivial ambiguities. It is passive and so doesn't require synchronization or a reference pulse. It is a variation of the very simple GRENOUILLE technique currently in common use [20]. GRENOUILLE has the advantages that, in its standard form, it comprises as few as only four simple optics, has no beam splitters or beam recombining optics and so is extremely easy to align, and does not require the use of extremely thin second-harmonic-generation (SHG) crystals, which can be difficult to manufacture and which limit device sensitivity.

Indeed, GRENOUILLE actually *requires* a thick crystal because, unlike traditional pulse-measurement devices, it uses the crystal phase-matching bandwidth for its spectral resolution [22], and the thicker the crystal the better the spectral resolution. The thick crystal also improves the device sensitivity. Indeed, the ps version of GRENOUILLE that we introduce here involves a several-cm crystal and so has particularly high-spectral resolution. Like previous GRENOUILLEs, it is also easily

aligned and, in fact, is composed of as few as only *three* simple optics, to our knowledge the simplest pulse-measurement technique ever developed.

In previous work, GRENOUILLE has measured Ti:Sapphire (700-1000nm) pulses from 20fs to ~1ps in length [23] and telecommunications pulses at 1.5 μm [24] over a similar pulse-length range. In addition, we have shown that GRENOUILLE also naturally measures pulse-front tilt and spatial chirp without any modifications [25]. Most recently, we have extended GRENOUILLE's spectral range to include pulses in the visible (460-740nm) [26], and we have found that it is much more resilient to beam-shape-induced distortions than traditional single-shot autocorrelators and FROGs [27].

GRENOUILLE has not yet, however, measured pulses longer than ~2ps. This is because the simultaneous need for both a large delay range and high spectral resolution is challenging. Here we solve these problems and extend GRENOUILLE to pulses as long as ~15ps. Our solution is the use of a unique, thick *pentagonal* SHG crystal. Also, we show that this GRENOUILLE can measure even complex pulses and here measure a pulse with a time-bandwidth product of 21. Finally, we consider GRENOUILLE's current limits with regard to long-pulse measurement.

2.2 GRENOUILLE and its extension to longer pulses

A pulse with a temporal length of Δt can exhibit spectral features as narrow as $\delta\omega \sim 2\pi/\Delta t$ wide, which must be resolved for an accurate measurement. Specifically, a 10ps pulse at 800nm has spectral features of ~0.1nm, so the required spectral resolution is ~0.05nm. In a GRENOUILLE, the spectral resolution is the crystal's phase-matching bandwidth, which is inversely proportional to the crystal thickness, so a thick and/or a dispersive

crystal is required. Additionally, a large delay range is required, which, for 10ps pulses, is ~20ps, or ~4mm separation in the crystal between the two pulse replicas, which is a large distance when simply crossing beams at an angle as is done in GRENOUILLE and other pulse-measurement devices in order to achieve the required delay range.

To achieve these goals, we make two device modifications. First, we use a several-cm-thick highly dispersive crystal ($LiIO_3$) to provide the required improved spectral resolution (see Fig. 2.1). Secondly, we use a very large beam crossing angle– more than twice as large as previous versions. This latter condition sounds easy, but in fact proved the most challenging task in designing this device. GRENOUILLE's convenience stems from its use of a Fresnel biprism to split the pulse into two and cross the resulting replicas without the need for any alignment (see Fig. 2.2). And it proved impossible to use it to achieve a large beam crossing angle.

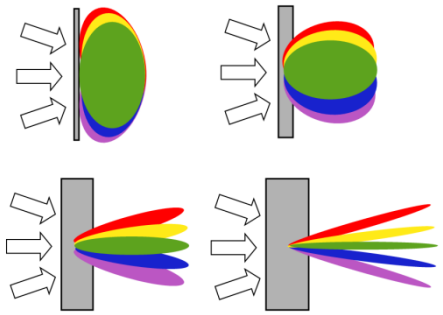

Fig. 2.1. Polar plots of SHG efficiency vs. output angle for various colors of a broadband beam impinging on a SHG crystal. Note that, for a thin crystal (upper left), the SHG efficiency varies slowly with angle for all colors, leading to a large phase-matching bandwidth for a given angle. As the crystal thickness increases, the polar plots become narrower, leading to very small phase-matching bandwidths. The thinnest crystal shown here would be required for all pulse-measurement techniques. GRENOUILLE, however, uses a thick crystal (lower

right) to spectrally resolve the autocorrelation signal, yielding a FROG trace — without the need for a spectrometer.

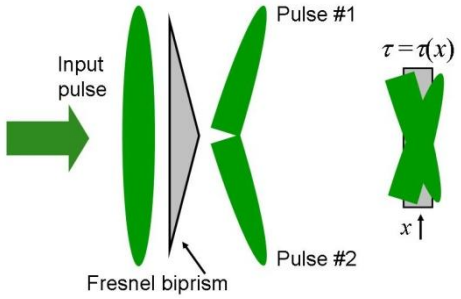

Fig. 2.2. Single-shot FROG measurements involve crossing large beams at a large angle, so that the relative delay between the two beams varies transversely across the crystal (right). The delay varies along *x*, the dimension in which the two beams are crossing. This can be accomplished more easily and without the need for alignment using a prism with a large apex angle (left).

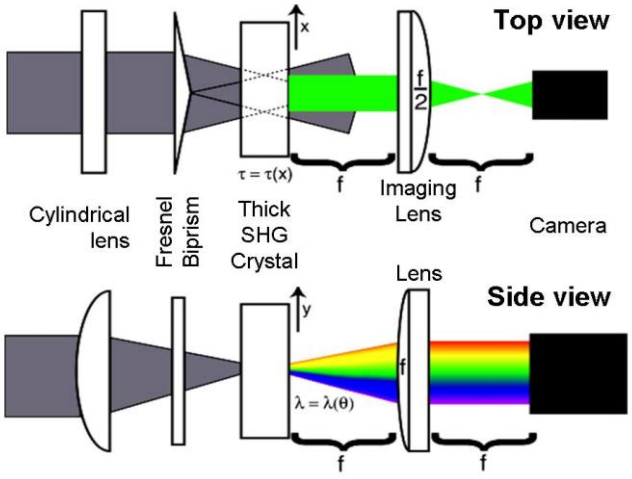

Fig. 2.3. Top and side views of GRENOUILLE. Use of the above anamorphic lens after the crystal yields a device with only four components.

The Fresnel biprism splits a 2cm beam into two 1cm-diameter beams, which, in order to attain a delay range of 20ps, requires a beam crossing angle of 30°. Unfortunately, a biprism in the geometries of Figs. 2.2 and 2.3 cannot accomplish this because total internal reflection occurs. Inverting the biprism so that it points toward the beam source might seem to solve this problem, but it yields beam overlap *inside the biprism*, not the SHG crystal.

To solve these problems, we modified the shape of the SHG crystal from the universally used rectangular shape to a *pentagonal* shape (see Fig. 2.4). This solves these problems and, even better, reduces the number of components in this already very simple device from four to as few as three (assuming a 2cm beam to begin with and an anamorphic lens after the crystal) [20], although in our first demonstration two lenses were used after the crystal, one for mapping wavelength to position and another for imaging the delay dimension.

Fig. 2.4 shows a schematic of the GRENOUILLE design used in this experiment. Our beam was small, so we expanded it using a cylindrical telescope in the horizontal dimension and then focused it onto the crystal by a cylindrical lens in the vertical dimension.

The pentagonal crystal splits the pulse into two separate beams and crosses them as shown in Fig 2.5(b), mapping delay onto horizontal position at the crystal and camera. The thick crystal phase-matches different colors for different angles in the other plane, which yields very small phase-matching bandwidths for the SHG beam. A vertical cylindrical lens then maps angle out of the crystal to vertical position at the camera, thus spectrally resolving the SHG beam in the vertical direction. The result is a single-shot

SHG FROG trace at the camera with delay varying in the x-direction and wavelength varying in the y-direction. Of course, many pulses can be averaged if desired.

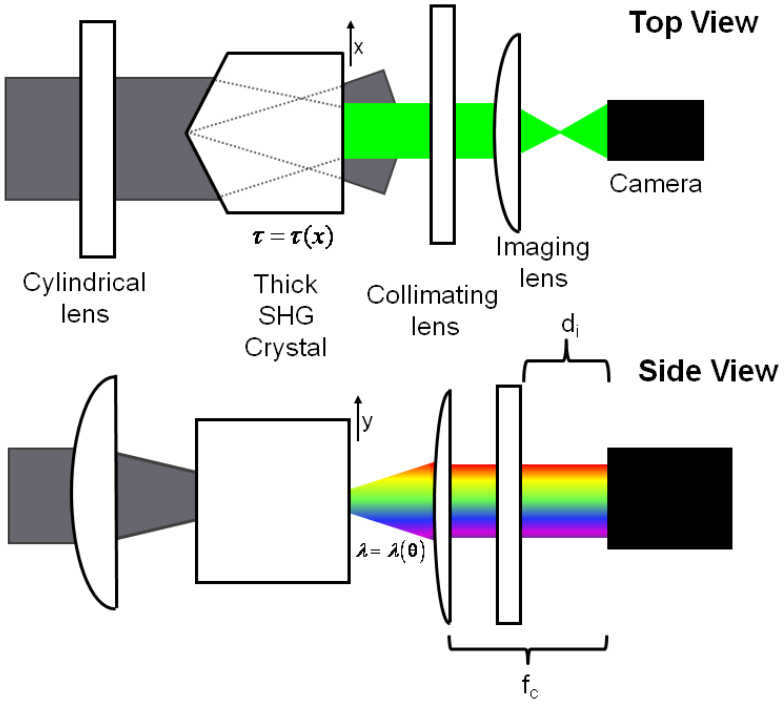

Fig. 2.4. The set-up for the ps GRENOUILLE. The schematic shows both the top view and the side view. The pentagon-shaped crystal both crosses the beams (top view) and angularly disperses the signal beam (side view). The collimating lens located a focal length, f_c, from the camera maps the angularly dispersed beam to position on the camera. The imaging lens is chosen to provide the depth of field necessary to image the entire width of the crystal. It is placed a distance d_i from the camera satisfying the imaging condition.

2.3 GRENOUILLE design

2.3.1 Crystal type and thickness

The first step in designing a GRENOUILLE for relatively long pulses is to determine the crystal type and thickness to yield sufficient dispersion to spectrally resolve the pulse. The use of a thick dispersive SHG crystal with high group velocity mismatch [GVM = $1/v_g(\omega) - 1/v_g(2\omega)$] results in a small phase matching bandwidth. This fact is embodied in the first important relation in GRENOUILLE theory:

$$GVM \cdot L >> \tau_p. \tag{2.1}$$

This relation places a lower limit on the spectral resolution of GRENOUILLE, where L is the crystal thickness and τ_p is the pulse width. Our device pushes Eq. (2.1) as far as possible, as described in [28]. In the experiments conducted in this paper a 4cm $LiIO_3$ crystal resulted in an upper limit of 23ps or the temporal range.

We cannot, however, increase GRENOUILLE's spectral resolution without limit by further increasing the thickness of the crystal. If the crystal is too thick, the input pulse will spread too much in time (distort) due to group velocity dispersion (GVD). This leads to the second important relation in GRENOUILLE theory:

$$GVD \cdot L << \tau_c, \tag{2.2}$$

where τ_c is the coherence length of the pulse, that is, its shortest temporal feature. Eq. (2.2) puts a lower limit on the temporal resolution of GRENOUILLE. In the experiments conducted in this paper, a 4cm $LiIO_3$ crystal resulted in a lower limit of 200fs on the temporal resolution. This yields a device finesse (the ratio of the temporal range and resolution) of 115, an excellent value for the measurement of even complex, shaped pulses.

2.3.2 Apex angle and width of crystal

The second step in designing our ps GRENOUILLE is to match the dispersion introduced by the crystal to both the apex angle and width of the pentagon-shaped crystal.

In the original GRENOUILLE design [20], the Fresnel biprism separates the initial beam into two identical beams and crosses them inside the crystal. Here we do so using a pentagonal SHG crystal.

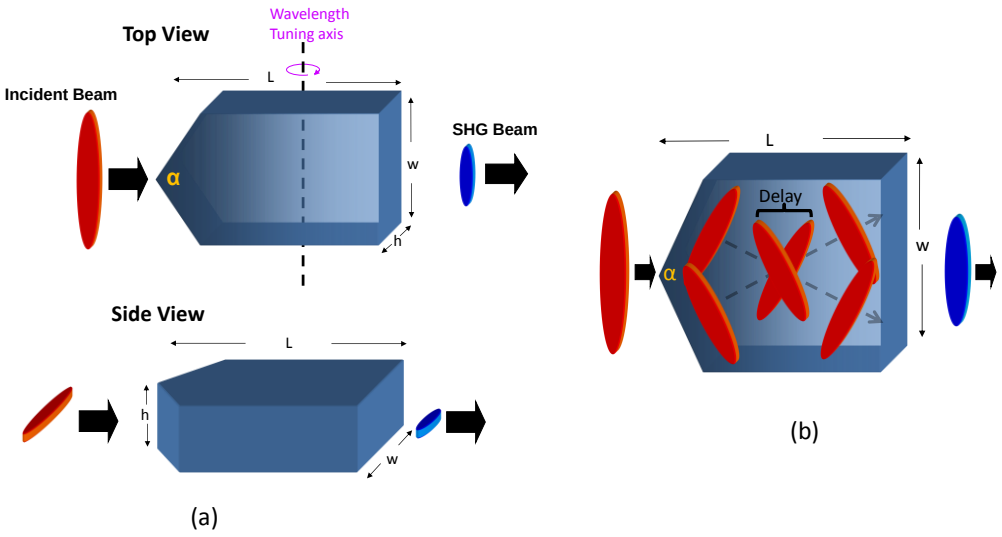

Fig. 2.5. a. The top and side views of the pentagonal SHG crystal. The top view also displays the axis about which the crystal can be rotated to tune the wavelength. b. The crossing of the signal beams inside of the crystal. This figure shows that by increasing the width of the beam, w, or the apex angle of the pentagon, α, the delay range is increased.

The pentagon shape forces the beams to begin crossing inside the crystal for all crossing/apex angles, thereby permitting a larger temporal range (see Fig. 2.5(b)).

Increasing the beam width, *w*, increases the spatial extent of the two beams inside the crystal and so also increases the temporal range of the device.

2.3.3 Matching the dispersion (crystal thickness) and the temporal range (apex angle and width)

Any temporal or spectral measurement device requires sufficient temporal and spectral range and resolution. By the fundamental nature of the Fourier transform, the spectral (and temporal) resolution required to resolve a pulse is the reciprocal of its pulse length (or spectral width) and vice versa. Thus, in a well-designed GRENOUILLE, the spectral resolution (phase-matching bandwidth) achieved by the crystal *and* the delay range should be related by the uncertainty relation. If this is not the case, the GRENOUILLE trace will be distorted. Either delay information at large delays will be lost while fine spectral features resolved, or the opposite instance, fine spectral features will be unresolved while information at large delays is recorded on the trace. Both situations will impede the performance of the FROG algorithm. Therefore the three parameters; length, width, and apex angle of the pentagon are related. The approximate spectral resolution of the crystal is the full-width-half-maximum of the phase-matching bandwidth [28]

$$\partial\lambda_{fwhm} = \frac{.44\lambda_0 / L}{\left| n'(\lambda_0) - \frac{1}{2} n'(\lambda_0 / 2) \right|}. \tag{2.3}$$

Because it provided the largest GVM for 800 nm, we chose a $LiIO_3$ crystal (cut at 60°). Additionally, we chose a very long thickness of 4cm. This provided $\delta\lambda_{fwhm}$ = .04nm, which is sufficient spectral resolution to resolve any spectral structure in a pulse with a pulse length of 23ps.

The temporal range, 23ps, determined by the spectral resolution, should also match the temporal range achieved by the crossing beams. Fig. 2.6 illustrates the ray tracing analysis of the beams inside the crystal.

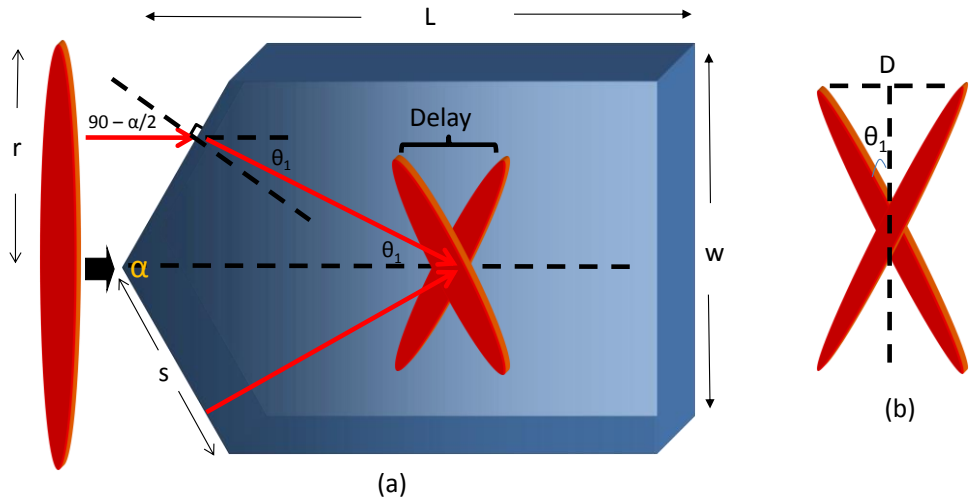

Fig. 2.6. a. The ray tracing diagram used to calculate the crossing angle of the two beams inside the crystal. b. The diagram used to calculate the range of delay inside the crystal.

The delay range of the GRENOUILLE depends on three parameters of the crystal, its apex angle, α; the index of refraction, n; and the width, w. First calculating the crossing angle, θ_1, we find using Fig. 2.6(a):

$$\theta_1 = 90 - \frac{\alpha}{2} - \sin^{-1}\left(\frac{1}{n}\cos\left(\frac{\alpha}{2}\right)\right). \tag{2.4}$$

Next, the maximum distance between the two edges of the crossing beams, D, shown in Fig. 2.6(b) is

$$D = s\sin\theta_1, \tag{2.5}$$

where s is the length of one of the beams inside of the crystal shown in Fig, 2.6(a), which, if the incident beam illuminates the entire width of the crystal, is

$$s = \frac{r}{\sin(\alpha/2)}. \tag{2.6}$$

The delay range is related to the maximum distance by

$$\Delta\tau = \frac{Dn}{c}, \tag{2.7}$$

where c is the speed of light in vacuum and n is the refractive index of the material.

Eq. (2.4-2.7) yield the expression for the delay range of the crystal,

$$\Delta\tau = \frac{r}{c}\cot\frac{\alpha}{2}\left(\sqrt{n^2 - \cos^2\left(\frac{\alpha}{2}\right)} - \sin\left(\frac{\alpha}{2}\right)\right). \tag{2.8}$$

In our experiment a 2.7cm wide type-I $LiIO_3$ crystal with an apex angle of 126° yielded a temporal range of $\Delta\tau_{range}$ = 19.5 ps.

A smaller apex angle, α, yields a larger crossing angle and hence a larger delay range, which appears to come at a cost of adding more potentially beam-distorting angular dispersion to the pulse. Fortunately, we find that the angular dispersion is negligible. But a smaller apex angle also yields a shorter beam overlap length, potentially smaller than the full crystal thickness, which would increase the phase-matching bandwidth. In addition, GRENOUILLE involves non-collinear SHG, and therefore is governed by the non-collinear SHG phase-matching condition:

$$n_e(2\omega) = n_o(\omega)\cos(\theta_1), \tag{2.9}$$

where θ_1 is the crossing angle of the two beams inside the crystal (Fig. 2.6). Due to the cosine, phase matching unfortunately can cease to be possible at large crossing angles, or in the case of GRENOUILLE, small crystal apex angles.

Although Eq. (2.9) shows that, by reducing the apex angle of the crystal, the index of refraction of the material can be changed, thereby modifying the value of the phase-

matching bandwidth given by Eq. (2.3), the dependence on the phase matching bandwidth and the crossing angle is negligible. Therefore, further reducing the apex angle of the crystal is *not* an effective way to increase the spectral resolution of GRENOUILLE unless the beam can be made larger and the noncollinear phase-matching condition can continue to be satisfied.

One characteristic of all GRENOUILLE designs is the effect of the spatial profile of the beam on the measured GRENOUILLE trace. This effect is simply a spatial intensity mask [29] and can be calculated from the measured spatial intensity profile of the beam. For longer pulses the spatial mask could reduce the intensity of features at large delays due to the beam intensity falling off at the crystal edges, which correspond to large delays. Such distortions can be removed by dividing the measured GRENOUILLE trace by the intensity mask. But, as has been shown previously, because GRENOUILLE uses such thick crystals, the beams cross through each other throughout the crystal, thus smearing out any distortions due to this effect, which is especially so for the current device, rendering this effect nearly irrelevant for this device, except for cases involving pulses as long as the time limit of the device that happen to have beam sizes that are too small [29].

Alternative crystal materials with high GVM values are listed below in Table 2.1 for other wavelength ranges at room temperature operation.

Table 2.1. Different possible crystal materials for varying wavelength ranges. The average GVM corresponds to the average GVM over the wavelength range [30].

Material	Wavelength Range (nm)	Average GVM (fs/cm)
$LiIO_3$	700-900	6923
$LiNbO_3$	900-1200	7162
Ag_3AsS_3 (Proustite)	1200-2500	6733

2.3.4 Depth of field

Another important aspect to consider when deciding upon the construction of a GRENOUILLE for measuring long pulses is the depth of field of the imaging system. In GRENOUILLE the depth of field of the imaging system must be approximately equal to or exceed the crystal thickness. If this condition is not met, fine trace structure will be out of focus and wash out [20].

Depth of field was not an issue in previous implementations of GRENOUILLE, which used crystals of thicknesses <5mm, because the depth of field requirement was met easily. However, as the thickness of the crystal increases, the depth-of-field requirement becomes more difficult to satisfy.

To check this condition for our device, assume that the crystal center is a distance d_o away from the lens and is perfectly imaged onto a camera a distance d_i from the lens.

Next, we consider a potentially out-of-focus front surface at a distance $\varepsilon+d_o$ from the lens, which will be acceptably in focus if

$$\varepsilon = 2d_o r_c / Md, \tag{2.10}$$

where r_c is the required spatial resolution at the camera, M is the magnification of the imaging system, and d is the diameter of the beam on the lens. In our experiment, using an imaging lens with a focal length of 150mm to image the crystal at an object distance of 600mm yielded a depth of field of 6.4cm. We experimentally determined the required spatial resolution to be roughly 50pixels or .175mm after performing a similar GRENOUILLE experiment and noting the delays at which the trace began to wash out.

2.3.5 Minimum pulse energy required for GRENOUILLE

An important parameter to consider is the pulse energy required for the modified GRENOUILLE to work.

The detector arrays for all GRENOUILLEs are cameras that are composed of pixels that register a number of counts proportional to the number of incident photons. Roughly 700 blue (400nm) photons are required to register a count of 100 on a 10-bit pixel in a CMOS camera array. Additionally, a FROG trace for a complex pulse may require a 128×128 array size. Therefore, a minimum of $700\times128^2 \sim 11$ million photons would be required to generate the trace, and the minimum energy required to generate the FROG trace would be

$$E_{min} = N\frac{hc}{\lambda} = 5.7\text{pJ} \tag{2.11}$$

where N is the number of photons. If the signal is time averaged over the frame rate (~30fps for standard CMOS cameras), a minimum average power, $P_{\min}$ = 190pW, is necessary to measure a complex pulse.

Next, this minimum power must be related to the power of the SHG signal beam, P_{SHG}, generated by the crystal. But before we can do that, P_{SHG}, must be written in terms of the parameters of the GRENOUILLE and laser source. The power of the SHG signal beam is

$$P_{SHG} = I_{SHG} w_x w_y \tau_p r, \tag{2.12}$$

where I_{SHG} is the intensity of the SHG beam, w_x is width of the crossing beams inside the crystal in the delay dimension (the value s in Fig. 2.6(a)), w_y is the focused size of the beam (Fig. 2.4, side view), τ_p is the pulse length, and r is the repetition rate of the laser. The intensity of the SHG beam is given by [1] as

$$I_{SHG} = \frac{8\pi^2 \eta_0 d^2 I_{in}^2 L^2}{\lambda^2 n^3}, \tag{2.13}$$

where $\eta_0 = c\mu_0$, c is the speed of light in vacuum, d is the d-coefficient of the crystal defined as $d = \chi^{(2)}/2$, L is the length of the crystal, λ is the fundamental wavelength, n is the index of refraction of the crystal, and I_{in} is the intensity of the input beam

$$I_{in} = \frac{E_{in}}{w_x w_y \tau_p}, \tag{2.14}$$

where E_{in} is the energy of the input pulse. Additionally, the length of the crystal, L, should be matched to the confocal parameter of the focused beam [20] resulting in the relation

$$L = \frac{2\pi w_y^2}{\lambda}. \tag{2.15}$$

Eq. (2.12-2.15) can be used to solve for the power of the signal beam

$$P_{SHG} = \frac{8\pi^2 \eta_0 d^2 E_{in}^2 L^{3/2} \sqrt{2\pi}}{w_x \lambda^{5/2} n^3 \tau_p} r. \tag{2.16}$$

Now that P_{SHG} is written in terms of the GRENOUILLE and laser source parameters, the minimum energy for GRENOUILLE can be determined. Using the minimum average power required for a FROG trace as P_{SHG} in Eq. (2.16), and solving for E_{in} yields the minimum energy required for GRENOUILLE to work

$$E_{min} = \sqrt{\frac{\lambda^{5/2} n^3 w_x \tau_p P_{min}}{8\pi^2 \eta_0 d^2 L^{3/2} r \sqrt{2\pi}}}. \tag{2.17}$$

In the experiments performed in this paper, L = 4cm, n ~ 1.9, λ = 800nm, τ_p ~ 10ps, d ~ 4.4pm/V [30], w_x ~ 1.2cm, and r = 76MHz which yields a minimum energy of $E_{\min}$ ~ .3pJ per pulse, or multiplying $E_{\min}$ by the repetition rate, r, determines the minimum average power, P ~ 25μW.

Note that, in a GRENOUILLE, the length of the crystal is determined by the spectral resolution required to measure the pulse. If we write the spectral resolution required to resolve the pulse as $\delta\omega \approx 0.5/(TBP\ \tau_p)$, and use Eq. (2.3), we see that the crystal length must be proportional to the pulse length. Substituting this result into Eq. (2.17), we find that the minimal average power measurable by a properly designed GRENOUILLE scales *inversely* with the fourth root of the pulse length. Although this is a weak dependence, it is somewhat unintuitively the case that, due to the various partially cancelling factors, the longer the pulse the more sensitive the GRENOUILLE—provided that a device can be designed.

2.4 Experiment

We performed measurements using a Coherent MIRA Ti:Sapphire oscillator and a Coherent Legend-F regenerative amplifier. The first experiment involved a 5ps double pulse from the MIRA, which emitted pulses centered at 802nm with a FWHM bandwidth of 2.5nm, a repetition rate of 76MHz, and pulse energy of 5.2nJ per pulse. The second experiment involved the measurement of a train of pulses. To generate the train of pulses, higher pulse energies were required. For this experiment, we used pulses from the Legend-F regenerative amplifier, centered around 800nm and filtered with a 3nm-wide bandpass filter. The Legend-F amplifier system emitted pulses at a repetition rate of 1kHz and pulse energies of 3mJ per pulse.

In all our experiments, the incident beam had an initial beam diameter of ~ 2mm, and it was magnified by a factor of 20 in the delay dimension in order to ensure uniform beam intensity over the entire face of the crystal. Then the beam was focused onto the pentagonal $LiIO_3$ crystal using a 100mm focal length cylindrical lens.

The crossing beams in the crystal were then imaged onto the camera by a single 150mm focal-length cylindrical lens. Additionally, a 400mm focal length cylindrical lens oriented perpendicular to the imaging lens mapped the crystal exit angle to position at the camera. For experimental simplicity, these two lenses are usually combined into one anamorphic lens, but we have used two here for flexibility in these proof-of-principle measurements. In the second experiment, using the Legend-F regenerative amplifier, a 300mm focal length lens was used to fit the entire 3nm bandwidth of the incident beam on the camera. Lastly, a blue low-pass filter removed the 800nm light from the SHG beam. A CMOS camera located 800mm away from the crystal collected the image.

2.5 Results and discussion

We performed two experiments to demonstrate our ps GRENOUILLE's capabilities. These measurements highlighted, not only its ability to measure the intensity and phase of complex ps pulses, but also its high spectral resolution relative even to a conventional high-resolution spectrometer.

In the first experiment using the MIRA laser, we measured a 5.5ps double pulse. The double pulse was created using a Michelson interferometer. Fig. 2.7 shows the measurement of a 5.5ps (separation) double pulse.

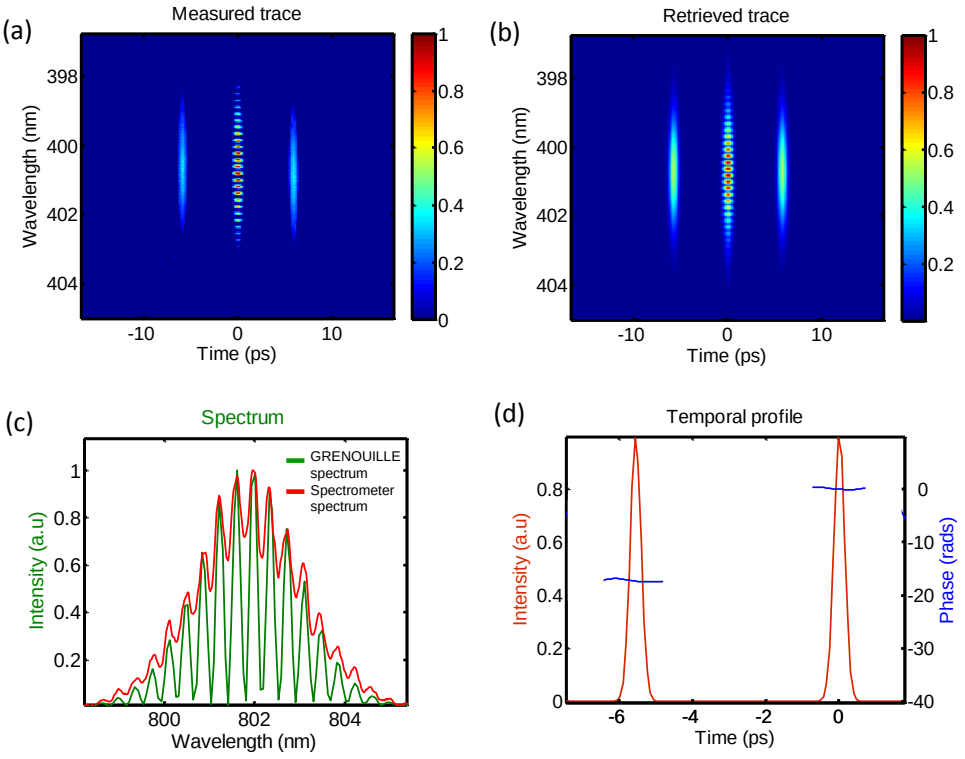

Fig. 2.7. a. The measured ps GRENOUILLE trace for a 5.5ps double pulse. b. The retrieved GRENOUILLE trace. c. The GRENOUILLE retrieved spectrum compared with that of a high resolution spectrometer with .01nm spectral resolution. The high contrast fringes demonstrate the high resolution of GRENOUILLE compared to a conventional

spectrometer. d. The retrieved temporal intensity and phase of the 5.5ps pulse. As expected, the retrieved temporal intensities of the pulses were equal.

To verify the accuracy of our measurement, we compared the GRENOUILLE-measured spectrum to that measured by a commercial high-resolution spectrometer with .01nm spectral resolution (Ocean Optics HR4000 spectrometer). The pulse's high-contrast fringes demonstrate GRENOUILLE's high spectral resolution compared to that of the commercial spectrometer. This high contrast—significantly better than our calculated value!—is a result of a combination of effects, including the thick crystal, the ability of the FROG algorithm to see otherwise washed out structure, and our deconvolution of the spectral response function from the results using a Lucy-Richardson deconvolution algorithm (a standard procedure in the GRENOUILE pulse-retrieval code [31]). This deconvolution algorithm functions to improve the spectral resolution without introducing any complexity to the device and is a commonly used procedure in image processing and spectral measurements [32], and it is standard in commercial GRENOUILLE software.

Next, we measured a train of pulses, made by passing the beam from the Coherent Legend-F through an etalon composed of two 90% partially reflecting mirrors. This measurement highlighted GRENOUILLE's ability to measure more complicated temporal and spectral profiles. Fig. 2.8(c) shows the agreement between the GRENOUILLE-retrieved spectrum and the spectrum measured by the spectrometer.

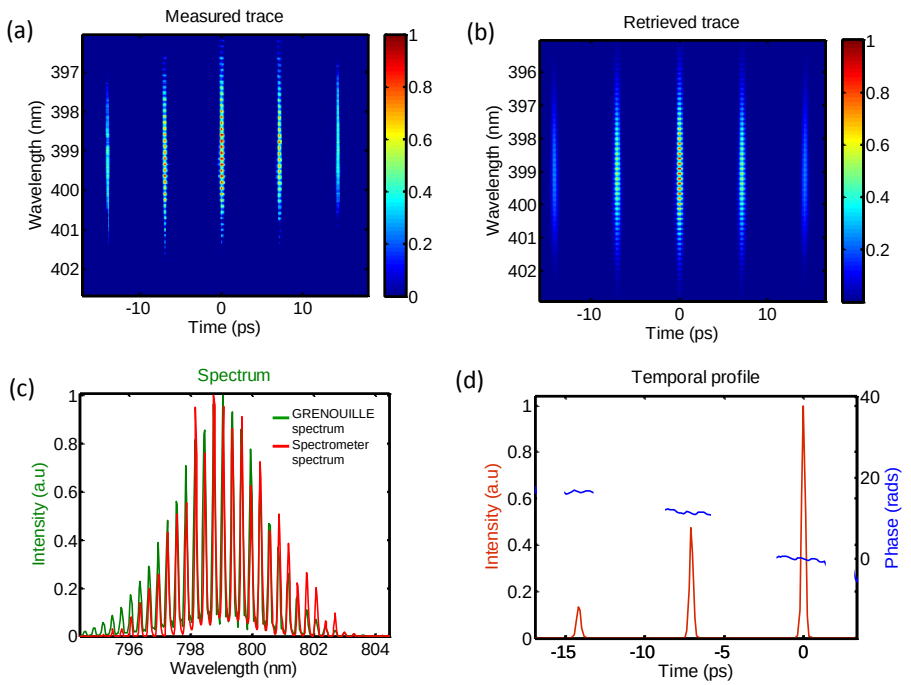

Fig. 2.8. a. The measured GRENOUILLE trace for a train of pulses. b. The retrieved GRENOUILLE trace. c. The GRENOUILLE retrieved spectrum compared with that of a spectrometer. The agreement between the two independent measurements confirms GRENOUILLE's capabilities. d. The retrieved temporal intensity and phase of the train of pulses.

Fig. 2.8(d) shows the retrieved temporal profile of the ~15ps train of pulses. As expected, the intensities of the pulses in the pulse train decreases with time because the pulse train was generated with an etalon composed of two 90% partially reflecting mirrors.

Although the temporal profile of the measurement in Fig. 2.8(d) is relatively simple, the spectral profile is complex, and GRENOUILLE should be capable of measuring pulses with even more complex temporal profiles, because the FROG algorithm has proven capable of measuring pulses with time-bandwidth products greater

than 1000 [14]. Our device, with its finesse of over 100, should be capable of measuring pulses with complexities (time-bandwidth products) up to almost this value.

To extend GRENOUILLE to even longer-pulse measurement would involve increasing the delay range by reducing the apex angle of the pentagon. While this yields a potentially shorter beam overlap region, a larger beam and corresponding larger width of the crystal could compensate for this effect. Use of a more dispersive crystal would also help; however, most applications for nonlinear crystals generally prefer less dispersive crystals, so such crystals may be difficult to obtain. As a result, a clever new idea would be preferable to achieve the measurement of even longer pulse lengths in a simple manner.

2.6 Conclusion

We have extended the GRENOUILLE technique for simple ultrashort-laser-pulse measurement to pulses up to ~15ps in length by replacing the Fresnel biprism and rectangular SHG crystal in the standard GRENOUILLE design with a single pentagonal SHG crystal. This reduces the number of components to as few as three (two lenses and the pentagonal crystal), making for an extremely simple, alignment-free device, whose convenience in pulse measurement seems unparalleled.

CHAPTER 3

VIPA/GRATING SPECTRAL INTERFEROMETRY

3.1 Introduction

In Chapter 2, we introduced a GRENOUILLE technique capable of measuring pulses up to ~20ps in length. But GRENOUILLE is incapable of measuring the type of very complex pulses used in OAWG because it is limited by its spectral range, spectral resolution, and sensitivity.

One very sensitive technique used to measure complex pulses is spectral interferometry (SI). SI is conceptually very simple: it involves simply measuring the spectrum of the sum of a known reference pulse and the unknown pulse. The pulses are aligned to have a separation in time of about five pulse lengths to yield spectral fringes which result in a simple pulse-retrieval procedure. Although the retrieval is simple, it comes at a price of spectral resolution. Indeed, it actually reduces the spectral resolution of the spectrometer used by a factor of 5. Therefore the simplest solution to increase the spectral resolution of SI, and employ the technique to measure OAWGs, is to use a high resolution spectrometer to measure the interferogram.

In this chapter we demonstrate to our knowledge the first implementation of SI using a virtually imaged phased array (VIPA) grating spectrometer [33] to measure pulses up to ~80ps (see Fig. 3.1). Additionally we theoretically model the VIPA spectrometer SI and detail its limitations for pulse measurement.

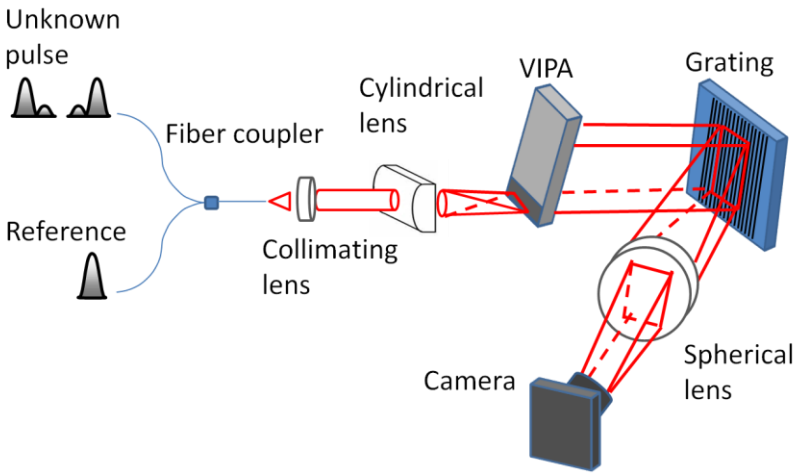

Fig. 3.1 The experimental setup for VIPA/grating SI. The unknown pulse and the reference pulse are incident upon a 3dB fiber coupler which ensures that both pulses are collinear at the input of VIPA/grating spectrometer. The output of the fiber coupler is collimated using a collimating lens and then focused in the vertical dimension onto the entrance (uncoated) region of the VIPA. The VIPA angularly disperses the beams in the vertical dimension. Since the beam is relatively broadband compared to the VIPA's free spectral range, multiple diffraction orders overlap in space. Therefore, the grating serves to spectrally resolve the beam in the horizontal dimension. The spherical lens located a focal length away from the camera maps angle to position and creates a 2-D spectral plot of the incident beams on the face of the camera.

3.2 VIPA/grating spectrometer SI theory

In this section we examine the theory governing VIPA/grating SI and explain the limitations in its accuracy and spectral resolution.

3.2.1 VIPA

A VIPA is a modified Fabry-Perot etalon. It consists of two glass plates of high reflectivity, typically ~100% on the input face and 99% on the output face. The physical difference between a VIPA and a conventional etalon is its uncoated entrance region for the input beam.

It is well known that etalons can be used as spectral filters as a result of the deconstructive interference that occurs upon the multiple reflections of the incident beam. For an etalon of width L, the total path length of the beam that undergoes m reflections is $\Delta x = 2Ln$, where n is the index of refraction of the etalon. Therefore, only wavelengths of light that satisfy the condition

$$\lambda m = 2Ln, \tag{3.1}$$

will result in constructive interference, while all other wavelengths will interfere destructively with the degree dependent upon the wavelength of the incident light.

Eq. (3.1) holds true for VIPA's as well as standard etalons. As shown in Fig. 3.1, a cylindrical lens is used to focus the incident beam into the entrance (uncoated region) of the VIPA. This focusing of the incident beam provides a range of incident angles which in turn results in a range of different path lengths, L, traveled during the multiple reflections, dependent upon the incident angle of each ray. Consequently, there are a range of different wavelengths which satisfy Eq. (3.1) and constructively interfere, and thereby, the VIPA angularly disperses the incident beam. And, by placing a thin lens a focal length away from the VIPA (see Fig. 3.2) we can make a VIPA spectrometer where the intensity distribution is governed by the equation [34]

$$I_{out}(x_F, \lambda) \propto e^{-\frac{2 f_c^{\,2} x}{f^2 W^2}} \times \frac{1}{(1-Rr)^2 + 4(Rr)\sin^2\left(\frac{k\Delta}{2}\right)} \tag{3.2}$$

where Rr is the product of the reflectivities of the highly reflective coatings of the VIPA, k is the wavenumber of the incident beam, f_c is the focal length of the cylindrical lens, f is the focal length of the second lens that maps angle to position on the camera plane, and W is the incident spot size of the beam on the first cylindrical lens.

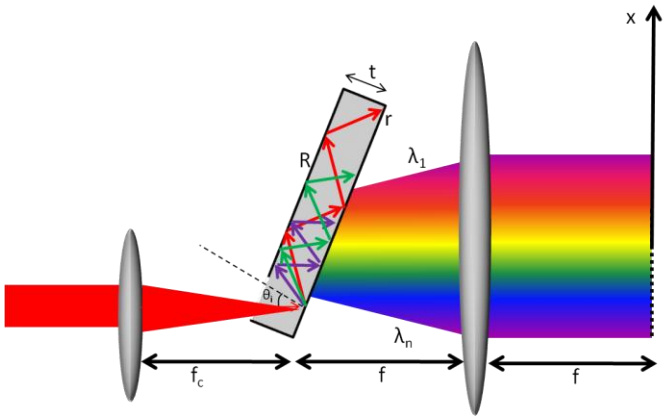

Fig. 3.2. The experimental set-up for a VIPA spectrometer. The incident beam is angularly dispersed by the VIPA and the lens located a focal length away from the input of the VIPA spectrally resolves the beam at the image plane of the detector.

Additionally, the parameter Δ is given by

$$\Delta = 2tn\cos\theta_{in} - 2t\frac{\tan\theta_{in}\cos\theta_i x}{f} - t\frac{\cos\theta_{in}x^2}{nf^2}, \tag{3.3}$$

where n*sin(θ_{in}) = sin(θ_i) (Snell's Law), and θ_{in} is the internal angle inside the etalon as a result of refraction.

The spectral dispersion law for VIPA can be derived from Eq. (3.2) and (3.3) yielding

$$m\lambda = \left[2tn\cos\theta_{in} - 2t\tan\theta_{in}\cos\theta_i\frac{x}{f} - \frac{t\cos\theta_{in}}{n}\frac{x^2}{f^2}\right]. \tag{3.4}$$

From Eq. (3.4) we can derive the wavelength spread as a function of position, x

$$\Delta\lambda_{VIPA} = \lambda_p - \lambda_0 = -\frac{\lambda_0}{n}\left[\frac{\tan\theta_{in}\cos\theta_i}{\cos\theta_{in}}\frac{x}{f} + \frac{1}{2n}\frac{x^2}{f^2}\right], \tag{3.5}$$

where $m\lambda_0 = 2t[\cos(\theta_{in})]$.

Eq. (3.5) shows that the distribution of wavelength spread over the detector is a nonlinear function of *x*. This is similar to that of a grating spectrometer which is governed by the well known dispersion law

$$m\lambda = d(\sin\theta_{ig} - \sin\theta_d), \tag{3.6}$$

where the θ_{ig} is the angle incident measured from the normal of the grating and θ_d is the diffracted angle measured from the normal. Yet for most instances experimenters are within the bounds of the paraxial approximation which results in the relation $\sin\theta_d \cong \frac{x}{f}$. And, we can solve for the wavelength spread as a function of position for the grating spectrometer

$$\Delta\lambda_g = \lambda_p - \lambda_0 = -\frac{d \cdot x}{f}. \tag{3.7}$$

Eq. (3.7) shows that under the paraxial approximation, the wavelength spread is linear for a grating. This is one of the reasons that gratings are commonly used as the dispersive elements for spectrometers. In contrast, Eq. (3.5) shows that in the paraxial approximation, the wavelength spread is nonlinear for a VIPA. But, if the nonlinear term is small compared to the linear term then the VIPA would provide a linear wavelength spread and could be effectively used as a spectrometer. In the following sub-section we detail the necessary parameters to attain an approximate linear dispersion from the VIPA.

3.2.2 VIPA as a linear wavelength disperser

To attain a relation necessary for a linear VIPA dispersion, Eq. (3.5) will be re-written. First, we set

$$\kappa = \frac{\tan\theta_{in}\cos\theta_i}{\cos\theta_{in}}, \tag{3.8}$$

and Eq. (3.5) becomes

$$\Delta\lambda_{VIPA} = -\frac{\lambda_0}{n}\frac{x}{f}\left[\kappa + \frac{1}{2n}\frac{x}{f}\right]. \tag{3.9}$$

Since the largest value of x will have the largest nonlinear factor, we take the maximum value of x to determine the condition for approximate linear wavelength dispersion, and we arrive at the inequality

$$1 >> \frac{x_{\max}}{2n\kappa f}. \tag{3.10}$$

For a 6mm CMOS detector (x_{max} = 3mm), a glass VIPA, an input angle of $\theta_i \sim 3°$, the right hand side of Eq. (3.10) is ~.1. For these parameters, Eq. (3.10) explains that the nonlinear component may not be negligible. Additionally, for a smaller angle of incidence the right hand side of the inequality becomes larger and therefore, the nonlinear terms in the wavelength dispersion are more pronounced.

For the experiments described in this paper we satisfy Eq. (3.10) and therefore, the VIPA functioned as a linear wavelength disperser similar to a grating spectrometer.

3.2.3 VIPA/grating spectrometer

For the VIPA/grating spectrometer, the VIPA disperses the beam in the x dimension while the grating is oriented such that it disperses in the y dimension. As a result it is safe to assume that the angular dispersion in x is independent to that in y, and the intensity distribution is the product of that from the VIPA and that from a grating [33]

$$I_{out}(x,\lambda) \propto I_{in}(\tilde{\omega}) \exp\left(-\frac{2 f_c{}^2 x}{f^2 W^2}\right) \times \frac{1}{(1-Rr)^2 + 4(Rr)\sin^2\left(\frac{k\Delta}{2}\right)} \exp\left(-\frac{(y-\alpha\tilde{\omega})^2}{w_0{}^2}\right) \quad (3.11)$$

where $w_0 = \frac{\cos(\theta_{ig})}{\cos(\theta_d)} \frac{f\lambda}{\pi W}$ is the focused beam waist in *y*, $\alpha = \frac{\lambda^2 f}{2\pi c d \cos\theta_d}$ is the grating dispersion parameter, $I_{in}(\tilde{\omega})$ is the input spectrum, and $\tilde{\omega} = \omega - \omega_0$ is the offset from the center frequency.

3.3 Experiment

We performed experiments using an Amplitude Systemes t-pulse 500 oscillator. The pulses were centered about 1026 nm with a FWHM bandwidth of ~2 nm, an average power of ~5W, and a pulse width of ~500fs.

The setup used in this experiment is shown in Fig. 3.1. The unknown pulse was generated using a homemade Michelson interferometer. Both the reference pulse and the unknown pulse were coupled into a 3 dB fiber coupler which ensured the two pulses were collinear incident upon the VIPA spectrometer. Next, a lens with a focal length of 25mm collimated the output of the fiber. The collimated beam was focused by a 40mm focal length lens onto the back face of the VIPA.

The VIPA used in this experiment had a width of 5mm which determined its free spectral range. From Eq. (3.4) the free spectral range can be derived to be

$$FSR = \frac{\lambda_0{}^2}{2tn\cos(\theta_{in})} = .04nm. \quad (3.12)$$

The front surface of the VIPA had a reflectivity, *R*, of ~100% and the back side had an *r* = ~99%. The beam was dispersed in the vertical dimension by the VIPA.

After the VIPA, a 1200 grooves/mm grating dispersed the beam in the horizontal dimension. Then a 400mm focal length spherical lens was used to map wavelength to position at the camera.

3.4 Results and discussion

We performed two experiments to demonstrate the unique capabilities of VIPA/grating SI compared to other pulse characterization techniques. In both experiments VIPA/grating SI provides the necessary spectral resolution to completely characterize the intensity and phase of the unknown pulse.

Before performing SI, we tested the VIPA/grating spectrometer and found excellent agreement with the expected results. Fig. 3.3 shows 3 spectral measurements using the VIPA/grating spectrometer.

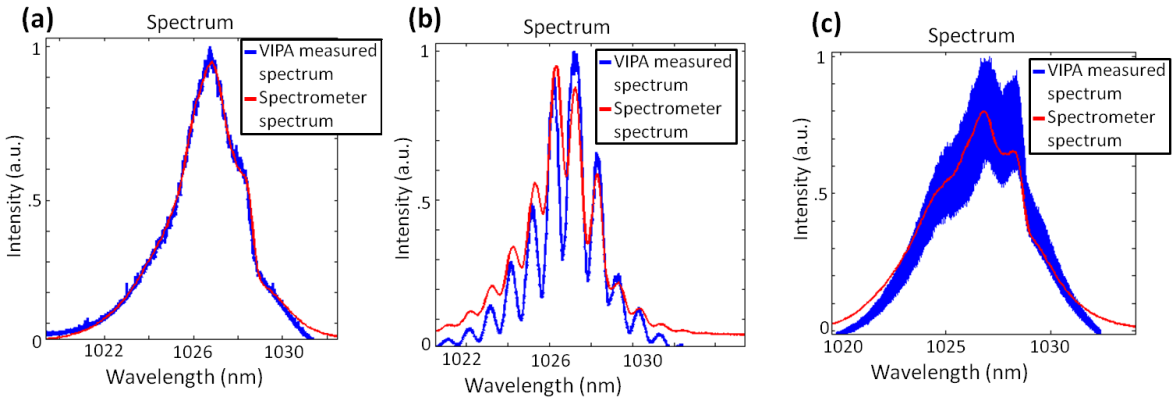

Fig. 3.3. The VIPA/grating spectrometer spectrum measurements (blue) compared to that of a grating spectrometer (red). a. The measurement of a single pulse. b. The measurement of a double pulse. c. The measurement of a very long double pulse. This measurement highlights the high spectral resolution of the VIPA/grating spectrometer. The fine spectral fringes due to the long pulse separation are resolved with the VIPA/grating spectrometer, while the grating spectrometer is not able to resolve such fine spectral features due to its limited spectral resolution.

Fig. 3.3(c) highlights the high spectral resolution of the VIPA/grating spectrometer. The fine spectral fringes due to the long pulse separation are resolved with the VIPA/grating spectrometer while the fringes are not present in the grating spectrometer measurement. Additionally, all the measurements displayed in Fig. 3.3 demonstrate that the VIPA/grating spectrometer produces the expected spectrum and therefore, the VIPA behaves as a linear spectral disperser. As a result, the inequality in Eq. (3.10) is satisfied as expected because the experimental parameters, x_{max} = .87mm, a glass VIPA, and an input angle of $\theta_i \sim 3°$, resulted in a value of .03 for the right hand side of Eq. (3.10). The small spatial range was due to the small FSR. The FSR could have been increased by using a thinner VIPA, but this would have resulted in less spectral resolution.

In the first experiment, we measured a double pulse consisting of two linearly chirped pulses separated by ~17ps (see Fig. 3.4).

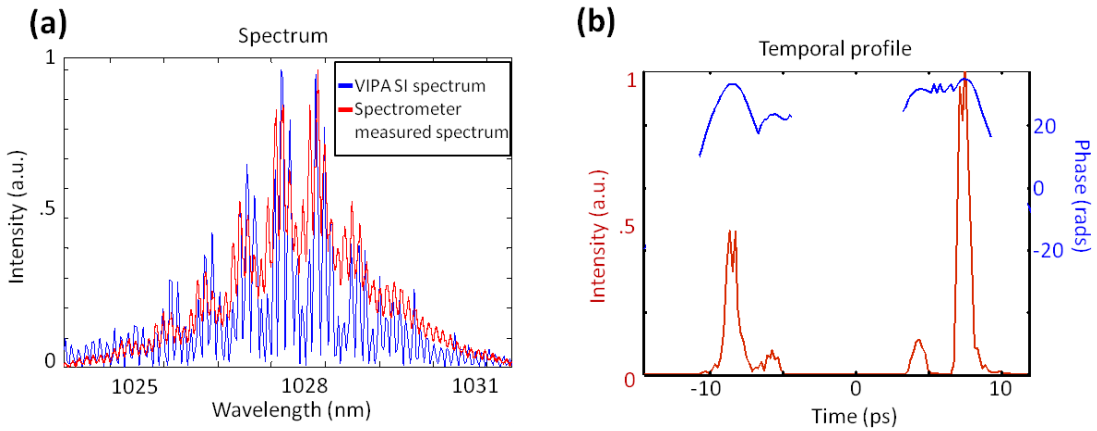

Fig. 3.4. a. The retrieved spectrum of a 17ps double pulse (blue) compared to a spectrum measured with a spectrometer. The high contrast of the VIPA/grating SI retrieved spectrum is clearly visible compared to the spectrometer measured spectrum. b. The retrieved temporal profile.

Fig. 3.4(a) shows the excellent agreement between the expected spectrum and that measured using VIPA/grating SI. Additionally, the high spectral resolution of VIPA/grating SI is demonstrated by the higher contrast spectral fringes shown in blue in Fig. 3.4(a). The temporal profile is displayed in Fig. 3.4(b). It shows two sets of double pulses. This is expected because the unknown pulse was generated from a Michelson interferometer in which the .6mm thick beam splitter used resulted in back reflections causing a trailing pulse behind the first pulse and in front of the second pulse. The measured temporal separation between the trailing and leading pulses was ~3ps which corresponds to a path length of ~.6mm in fused silica which is in agreement with the measured thickness of the beam splitter, ~.6mm.

In the second experiment, we measured a double pulse consisting of two linearly chirped pulses separated by ~80ps (see Fig. 3.5).

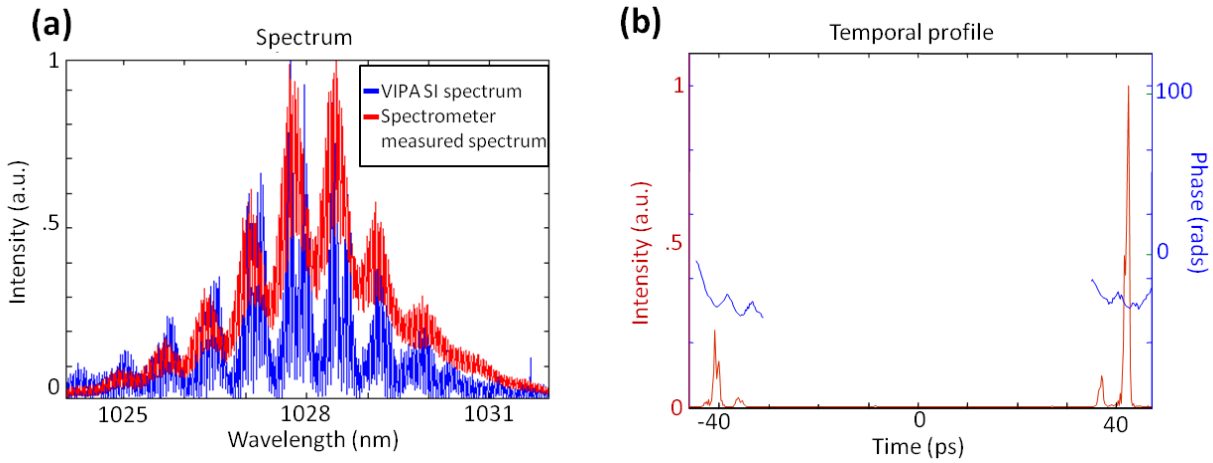

Fig. 3.5. a. The retrieved spectrum of an 80ps double pulse (blue) compared to a spectrum measured with a spectrometer. The high contrast of the VIPA/grating SI retrieved spectrum is clearly visible compared to the spectrometer measured spectrum. b. The retrieved temporal profile.

Fig. 3.5(a) shows the excellent agreement between the expected spectrum and that measured using VIPA/grating SI. Again, the high spectral resolution of VIPA/grating SI is demonstrated by the higher contrast spectral fringes shown in blue in Fig. 3.4(a). The temporal profile is displayed in Fig. 3.4(b). As expected, it shows two sets of double pulses.

3.5 Conclusion

We have demonstrated a variation of SI using a VIPA/grating spectrometer used to measure pulses up to 80 ps in length. To our knowledge this is the longest pulse every measured using Fourier transform spectral interferometry, and the first use of a VIPA spectrometer for spectral interferometry.

CHAPTER 4

MULTIPLE-DELAY CROSSED-BEAM SPECTRAL INTERFEROMETRY: MUD TADPOLE

Portions of this work appear in [35], J. Cohen, P. Bowlan, V. Chauhan, and R. Trebino, "Measuring temporally complex ultrashort pulses using multiple-delay crossed-beam spectral interferometry," Opt. Express **18**, 6583-6597 (2010).

4.1 Introduction

In Chapter 3, we introduced a variation of SI which significantly increased its spectral resolution and permitted the measurement of pulses up to ~80ps in length. Yet, the spectral resolution/temporal range is limited by the nonlinear spectral dispersion and the spectral resolution of the VIPA/grating spectrometer.

In this chapter we introduce a SI technique that is not limited by the spectral resolution or the nonlinear dispersion (at least not to the extent of a VIPA/grating spectrometer). As a result, it is capable of measuring pulses with pulse lengths of several ns with fs temporal resolution.

Ordinarily, such a method would require a high-resolution spectrometer, but our method overcomes this need. It involves making multiple measurements using SI (in its SEA TADPOLE variation [36]) at numerous delays, measuring many temporal pulselets within the pulse, and concatenating the resulting pulselets. Its spectral resolution is the inverse delay range—many times higher than that of the spectrometer used. Our simple proof-of-principle implementation of it provided 71 fs temporal resolution and a temporal range of 100 ps using a few-cm low-resolution spectrometer.

Here we extend the temporal range of SEA TADPOLE to measure the complete temporal intensity and phase of even longer and more complex waveforms. Rather than using a reference pulse at just one delay, as in standard SI and SEA TADPOLE, we use *many delays*, making SEA TADPOLE traces for all temporal slices of the long pulse and then concatenate them to reconstruct the entire pulse in time. We call this technique MUltiple Delay for Temporal Analysis by Dispersing a Pair of Light E-fields (MUD TADPOLE). The effective spectral resolution of MUD TADPOLE is many times that of SEA TADPOLE, and it is independent of the spectral resolution of the spectrometer. Instead, the spectral resolution is equal to the reciprocal of the reference-pulse delay range. In other words, it can measure pulses as long as the delay that can be generated. Since it is much easier to generate delay than to improve spectral resolution, this is a significant advantage, akin to that of Fourier-transform spectrometers over grating spectrometers, but without the stringent alignment issues.

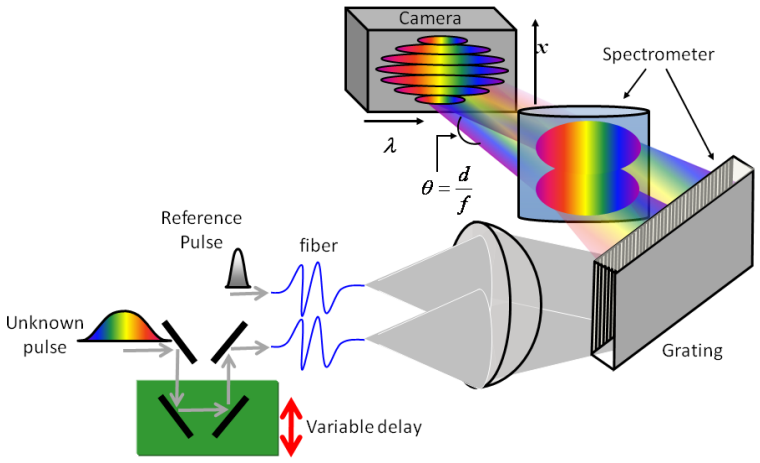

Fig. 4.1. Experimental setup for MUD TADPOLE. Both the unknown pulse and the reference pulse are coupled into two equal-length single-mode fibers. The unknown pulse passes through a delay stage, which provides the variable delay. Although here it is shown that the unknown pulse is delayed with respect to the reference, it is

inconsequential which pulse is delayed with respect to the other. In the horizontal dimension, the light is collimated by the spherical lens and spectrally resolved by the spectrometer. In the vertical dimension, the beams cross at a slight angle resulting in spatial fringes at the camera.

Indeed, MUD TADPOLE (see Fig. 4.1) is easily aligned and places no constraints on the pulse being measured (except for SI's usual condition that the reference pulse spectrum contain that of the unknown pulse). Using a simple Fourier-filtering algorithm, MUD TADPOLE directly retrieves both the intensity and phase of the unknown pulse. Additionally, it can in principle be easily extended to measure extremely complex nanosecond long pulses with fs resolution, achieving temporal range-to-temporal resolution ratios of ~ 210,000, while measuring complex pulses with time-band-width products of ~ 70,000.

Although the version of MUD TADPOLE that we discuss here is a multi-shot technique, we believe that the long temporal range, or equivalently its high spectral resolution, provides a substantial improvement to the field of arbitrary waveform metrology.

4.2 MUD TADPOLE: Extending SEA TADPOLE to longer pulses

The condition that the length of a pulse measured by SEA TADPOLE is limited to the inverse spectral resolution of the spectrometer can also be expressed in terms of the temporal length of the reference pulse at the *output* of the spectrometer. A fundamental, but often overlooked, property of spectrometers is that they stretch ultrashort pulses [37]. This has been experimentally verified for ps pulses [38] and fs pulses [39] by measuring the pulse at the output of a spectrometer.

This is easily understood by considering that spectrometers map a small range of frequencies, $\delta\omega$, equal to the spectral resolution, to each pixel of the detector. From the uncertainty principle, such a narrow band of frequencies can only be contained in a pulse that has a temporal duration:

$$\tau_{sp} \geq \frac{1}{\delta\omega}. \tag{4.1}$$

Therefore, the reference pulse broadens in time inside the spectrometer by the reciprocal of the spectrometer's spectral resolution, τ_{sp}. Because SEA TADPOLE (and other SI techniques) requires the formation of fringes, it also requires temporal overlap of the reference and unknown pulses. Thus it can, at best, be used to measure a pulse only τ_{sp} long. (In principle, the same broadening occurs to the unknown pulse, but the unknown pulses of interest here are, by assumption, already as long as, or longer than, τ_{sp}, so their temporal duration is assumed to be negligibly broadened by the spectrometer.)

In order to measure longer pulses, SEA TADPOLE must be outfitted with a higher resolution spectrometer, which would yield a longer τ_{sp}. Unfortunately, high-resolution spectrometers are extremely large, inconvenient, and expensive due to the proportional relationship between a spectrometer's spectral resolution and number of grooves illuminated on the grating (and hence its size).

Instead of using a high-resolution spectrometer, we introduce a technique that uses a delay stage to scan the unknown pulse in time, resulting in multiple SEA TADPOLE measurements at different delays. Each SEA TADPOLE measurement retrieves a different temporal section of the electric field of the unknown pulse, where the range of each individual measurement is $\tau_{sp,}$ and is much shorter than the unknown pulse duration. The retrieved spectral fields are then Fourier transformed to the time domain

yielding the retrieved section of the unknown pulse in time. Lastly, the retrieved sections are concatenated in time to reconstruct the entire unknown pulse.

4.3 MUD TADPOLE retrieval algorithm

The MUD TADPOLE retrieval algorithm (see Fig. 4.2) consists of three parts, a spatial Fourier-filtering step, a temporal filtering step, and concatenation.

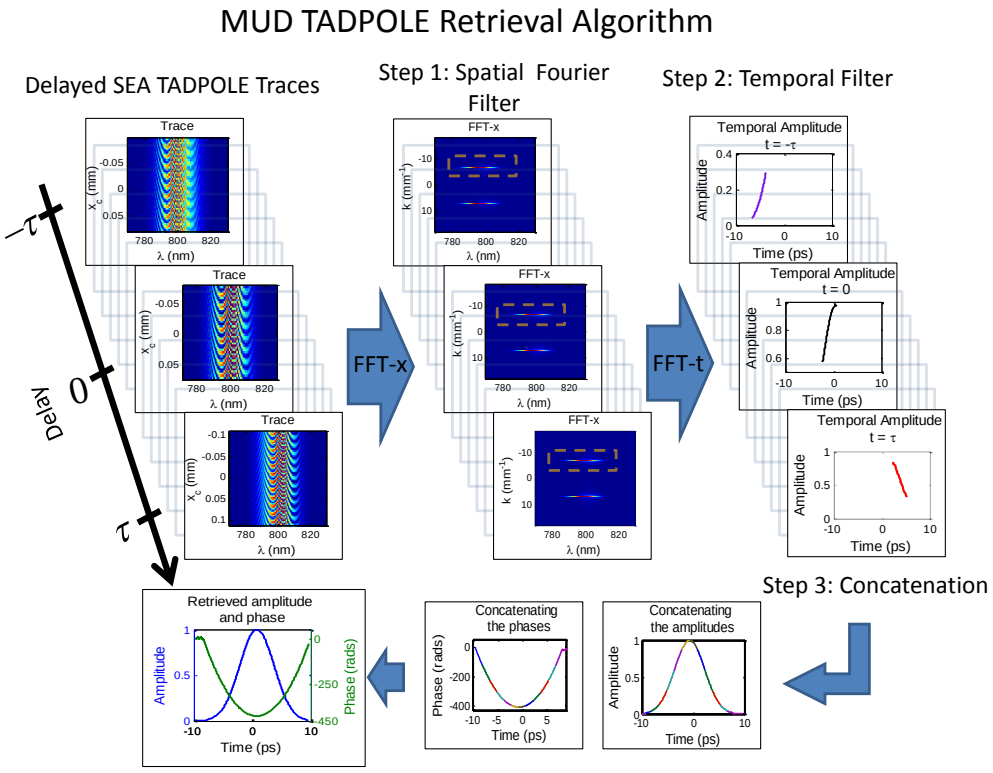

Fig. 4.2. The MUD TADPOLE retrieval algorithm using simulated data. In Step 1, each SEA TADPOLE trace—corresponding to a different temporal slice—is spatially Fourier filtered, resulting in the electric field at each delay, $E_i(\omega)$. In Step 2, the retrieved fields are temporally filtered, keeping only the region in which the unknown and reference pulses are temporally overlapped. Each retrieved field, $E_i(\omega)$, is Fourier transformed to the time domain and temporally shifted to the lab frame yielding $\tilde{E}_{i,lab}(t-\tau_i)$. In the figure,

each color represents the retrieved field at a different delay. Although, only the amplitudes are shown, after re-phasing, the same process is done with the retrieved phases. In Step 3, the retrieved amplitude and phase are separately concatenated using a weighted average, resulting in the retrieval of the entire unknown pulse.

4.3.1 Spatial Fourier filtering

The first step of the MUD TADPOLE pulse-retrieval algorithm is identical to the SEA TADPOLE Fourier-filtering algorithm [36, 40]. In SEA TADPOLE, the electric field of the unknown pulse is retrieved from a spectrally resolved spatial interferogram resulting from the crossing of two beams. The interferogram is given by the following equation:

$$S(x_c,\omega) = S_{ref}(\omega) + S_{unk}(\omega) + 2\sqrt{S_{ref}(\omega)}\sqrt{S_{unk}(\omega)}\cos(2kx_c \sin\theta + \varphi_{unk}(\omega) - \varphi_{ref}(\omega)), \qquad (4.2)$$

where θ is half the beam crossing angle, and x_c is the spatial coordinate along the crossing dimension shown in Fig. 4.1.

The entire electric field of the unknown pulse, consisting of both the phase and spectral amplitude can be retrieved from Eq. (4.2) by isolating the argument and amplitude of the cosine term. This is done by applying a one-dimensional Fourier transform along the x_c-dimension [36, 40]. Once in k-space, the phase and non-phase information (the first two terms in Eq. (4.2)) from the interferogram separate out as illustrated in Fig. 4.3(b). Either of the side-bands is isolated from the rest of the data and then Fourier transformed back to the position domain. This results in the product of the unknown and reference pulse complex fields. Additionally, using FROG, the phase of the field of the reference pulse must be measured, and divided out, thereby completely characterizing the unknown pulse.

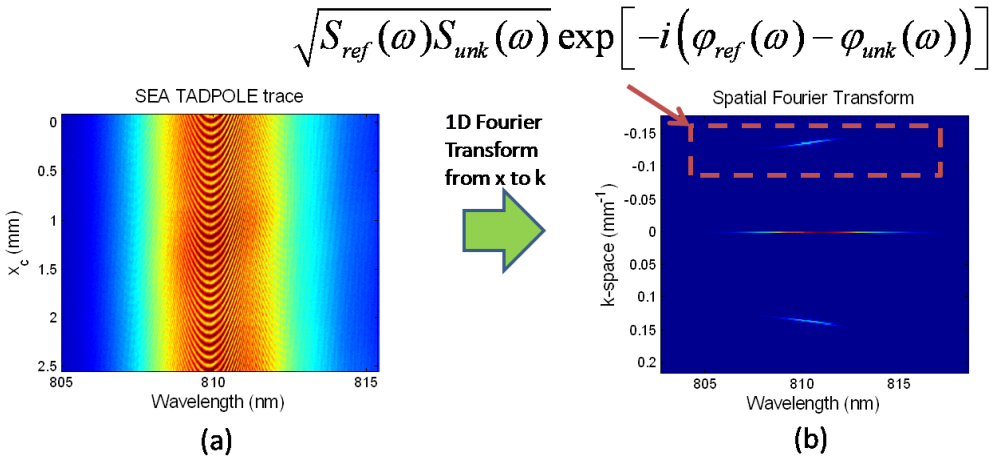

Fig. 4.3. Retrieving the phase and spectrum in SEA TADOLE. a. A SEA TADPOLE trace of a heavily chirped pulse. b. The one-dimensional spatial Fourier transform separates the data into three bands. The side-bands contain both the spectral phase difference and the spectrum of the unknown pulse, and so one of these is kept, and then inverse Fourier transformed back to the position domain. Due to the fibers, no spatial information about the pulse is present, so we sum the resulting field over the camera's position axis. At this point, the known reference pulse's field is divided out in order to extract the unknown pulse's intensity and phase.

A typical MUD TADPOLE data set consists of N SEA TADPOLE traces like the one shown in Fig. 4.3(a). Figure 4.2 illustrates the multiple SEA TADPOLE traces. Since the reference pulses are successively delayed in time by a constant, τ_{ref}, each retrieved spectrum, $S_i(\omega)$, and spectral phase difference,

$$\Delta\varphi_i(\omega) = \varphi_{unk_i}(\omega) - \varphi_{ref_i}(\omega), \tag{4.3}$$

corresponds to a measurement of the unknown pulse at a different time, τ_i. Here τ_i is the delay between the reference and unknown pulse for the i^{th} SEA TADPOLE trace. Each SEA TADPOLE trace combined with a FROG measurement of the reference pulse determines the spectral phase of the unknown pulse, $\varphi_{unk}(\omega)$, yielding the entire electric field,

$$E_i(\omega) = \sqrt{S_i(\omega)} e^{i\varphi_i(\omega)}. \tag{4.4}$$

At the spectrometer, the duration of each reference pulse in time is given by τ_{sp}. Each reference pulse interferes with the unknown pulse over a temporal width of τ_{sp}. Therefore, each $E_i(\omega)$, will contain spectral information about the unknown pulse in the time window,

$$\tau_i - \frac{\tau_{sp}}{2} < t < \tau_i + \frac{\tau_{sp}}{2}. \tag{4.5}$$

Therefore, the first step of the MUD TADPOLE retrieval algorithm yields N measurements of the electric field of the unknown pulse centered about different times, $E_{i=1:N}(\omega)$.

4.3.2 Temporal filter

The second step of the MUD TADPOLE algorithm involves temporal filtering each of the N measurements described above. In this step, the retrieved electric fields are Fourier transformed from the spectral domain into the time domain. This results in electric fields centered about each τ_i. Because the reference pulse interferes with a section of the unknown pulse of length τ_{sp}, which is smaller than the time-axis of the retrieved pulse, only information within this region is kept while that from larger and smaller times is discarded. Specifically, we crop each field so that:

$$\tilde{E}_i(t) = \begin{cases} \tilde{E}_i(t) & \text{for } \tau_i - \frac{\tau_{sp}}{2} < t < \tau_i + \frac{\tau_{sp}}{2} \\ 0 & \text{otherwise} \end{cases}. \tag{4.6}$$

After temporally filtering, each retrieved electric field is shifted in time because the field retrieved by the i^{th} reference pulse, $\tilde{E}_i(t)$, is centered around $t = 0$, the local zero

time value of the reference pulse. In other words, the i^{th} retrieved field, $\tilde{E}_i(t)$, is measured in a time frame relative to the i^{th} reference pulse. Since the goal of MUD TADPOLE is to piece together the entire unknown pulse in time, the retrieved fields must be transformed from the local time frame of each reference pulse to the lab frame in which all of the reference pulses occur at different times. This means that the i^{th} retrieved field, $\tilde{E}_i(t)$, is linearly shifted by τ_i,

$$\tilde{E}_i(t) \Rightarrow \tilde{E}_{i,lab}(t-\tau_i). \tag{4.7}$$

4.3.3 Concatenation

Although the spectrum and phase of the pulses from the mode-locked laser are quite stable, slight non-uniformity of the spatial fringes over a significant period of time, noise, and shot-to-shot jitter of the reference pulses cause discontinuities when concatenating the fields. To reduce these discontinuities we use a weighted averaging scheme.

Since each $\tilde{E}_{i,lab}(t-\tau_i)$ corresponds to an independent measurement by the i^{th} reference pulse from the laser, each retrieved field is weighted by a Gaussian weighting function with a half width at 1/e, τ_G, which is less than τ_{sp} and centered on the i^{th} reference pulse

$$G_i(t-\tau_i) = \exp\left[-\left(\frac{t-\tau_i}{\tau_G}\right)^2\right]. \tag{4.8}$$

The weighting function was chosen to be a Gaussian function because the temporal response function is approximately Gaussian in form [39, 41].

The accuracy of the experimental results are unaffected by variation of the width of the Gaussian weighting function as long as the width is less than τ_{sp}, and greater than

or equal to the delay spacing between the reference pulses, τ_{ref}, or,

$$\tau_{ref} \leq \tau_G < \tau_{sp}. \tag{4.9}$$

Because the delay between reference pulses, τ_{ref}, is less than τ_{sp}, a given section of the unknown pulse is reliably retrieved by more than one reference pulse. Therefore, we average together this redundant information to obtain a better retrieval. But due to the spectrometer's finite resolution, the accuracy of an individual measurement decreases as you move away from its temporal origin. The purpose of the weighting function is to account for this. Therefore, we choose the weighting function to be Gaussian (rather than square) so that it more heavily weighs information that originates from the temporal center of the individual measurements. And keeping the weighting function's width less than τ_{sp}, assures that no information from delays greater than τ_{sp}, are included in the average, because this information is outside the spectrometer's temporal window and therefore, not accurate. This process reduces the noise in the retrieval and helps to avoid discontinuities when concatenating the independent measurements together.

Since τ_{sp} is directly related to the spectral resolution of a spectrometer, it can be obtained by measuring the fringe contrast of interference spectra at different delays [18, 42]. In our experiment we measured τ_{sp} = 9.2 ps. Therefore, using a delay spacing of τ_{ref} = 1.46 ps satisfied the condition that $\tau_{ref} < \tau_{sp}$.

Finally, the retrieved fields are concatenated together. We do this by separating each $\tilde{E}_{i,lab}(t-\tau_i)$ into its constituent phase and amplitude,

$$\tilde{E}_{i,lab}(t-\tau_i) = A_i(t-\tau_i)e^{i\varphi_i(t-\tau_i)}. \tag{4.10}$$

Before concatenating the phase, each measured phase, $\varphi_i(t\text{-}\tau_i)$, must be re-phased (that is, its zeroth-order phase value is matched to that of the neighboring pulselet). The

reason for this is that our interferometer is not actively stabilized. Therefore, there is a slow drift in the phase over the course of an entire MUD TADPOLE scan, just as there is in SEA TADPOLE [36, 43].

Accordingly, the retrieved temporal phases have a different absolute phase, which must be removed before concatenation. This can be done easily because the temporal sections of the unknown pulse measured by subsequent reference pulses overlap. Therefore, the absolute phase of two individual measurements of the same time are set equal, which effectively removes the effect of drift in MUD TADPOLE.

This re-phasing procedure uses the fact that the absolute temporal phase does not contain any frequency vs. time information [1]. Therefore, before concatenating, the absolute phases, $\varphi^{(0)}_i$, where,

$$\varphi_{i+1}\left(t-\tau_i\right)=\varphi_i^{(0)}+\varphi_i^{(1)}\left(t-\tau_i\right)+\varphi_i^{(2)}\left(t-\tau_i\right)^2+..., \tag{4.11}$$

are re-phased. Specifically, the absolute phase of the i^{th}+1 retrieved field, $\varphi^{(0)}_{i+1}$, is set equal to that of the previous retrieved phase at the midway point between the two, or:

$$\varphi_{i+1}^{(0)}\left(\frac{\tau_{i+1}+\tau_i}{2}\right)=\varphi_i^{(0)}\left(\frac{\tau_{i+1}+\tau_i}{2}\right). \tag{4.12}$$

This re-phasing is performed sequentially, beginning with φ_2 and ending with φ_N.

After re-phasing, both the phases, $\varphi_i(t-\tau_i)$, and amplitudes $A_i(t-\tau_i)$, are separately superposed using a weighted average, yielding the entire temporal amplitude of the unknown pulse:

$$A_{final}(t)=\frac{\sum_{j=1}^{N}G_j(t-\tau_j)A_j(t-\tau_j)}{\sum_{i=1}^{N}G_i(t-\tau_i)}, \tag{4.13}$$

$$\varphi_{final}(t) = \frac{\sum_{j=1}^{N} G_j(t-\tau_j)\varphi_j(t-\tau_j)}{\sum_{i=1}^{N} G_i(t-\tau_i)}. \quad (4.14)$$

The product of the amplitude and phase yields the entire temporal amplitude and phase of the unknown pulse.

$$\tilde{E}_{final}(t) = A_{final}(t)e^{i\varphi_{final}(t)}. \quad (4.15)$$

Figure 4.2 graphically represents the MUD TADPOLE retrieval algorithm.

4.4 Experimental setup

We performed experiments using a Coherent MIRA Ti:Sapphire oscillator. The pulses were centered at 805 nm, with a FWHM bandwidth of 6 nm. Using a Swamp Optics GRENOUILLE 8-50USB [20], the input pulse was measured to have a temporal width of 168 fs. The pulses were stretched to a FWHM length of 40 ps using a single-grating pulse compressor [13].

The SEA TADPOLE set-up shown in Fig. 4.1 is described in more detail in [36]. Specifically, for our set-up we used a 250 mm focal-length spherical lens to collimate and cross the beams emanating from the fibers. Additionally, a 600 grooves/mm grating and 200 mm focal-length lens were used for mapping wavelength to position in the spectrometer. The delay stage used was a Newport MFA Series Miniature Linear Stage with a Newport ESP100 single-axis controller.

4.5 Results and discussion

We performed two experiments to demonstrate MUD TADPOLE's unique capabilities relative to a conventional high-resolution spectrometer and to SEA TADPOLE. These experiments demonstrate how MUD TADPOLE overcomes the limitations of a conventional spectrometer as well as those of SEA TADPOLE. In both experiments MUD TADPOLE provides the necessary spectral resolution to completely characterize the intensity and phase of the unknown pulse.

In the first experiment, we measured the stretched 40 ps pulse using MUD TADPOLE with 100 SEA TADPOLE traces each having a different reference-pulse delay using the set-up shown in Fig. 4.1. The reference pulses were separated in time by 1.46 ps. This temporal spacing was chosen to provide a significant amount of overlap with neighboring reference pulses, thereby reducing discontinuities during the concatenation routine, which is helpful, but not necessary. The half width at 1/e of the weighting function was chosen to be equal to the temporal separation of the reference pulses, τ_G = 1.46 ps.

Figure 4.4(a) shows the retrieved temporal amplitude and phase of the 40 ps pulse. Since there is no commercial device capable of measuring the full intensity and phase of such a pulse, we compared the retrieved spectrum to that of an Ocean Optics HR 4000 spectrometer shown in Fig. 4.4(b). In this instance, the spectrometer provided enough spectral resolution to accurately measure the relatively smooth spectrum of the pulse. This is because the pulse compressor modifies the spectral phase rather than the spectral intensity. The result is that the linearly chirped pulse did not have finer spectral intensity features than the resolution of the spectrometer. Instead, the spectral phase of

the chirped pulse contained the fine spectral features, which the spectrometer is unable to measure. In contrast, MUD TADPOLE is able to measure the phase, as demonstrated by the complete measurement of the temporal intensity and phase of the 40 ps pulse shown in Fig. 4.4(a).

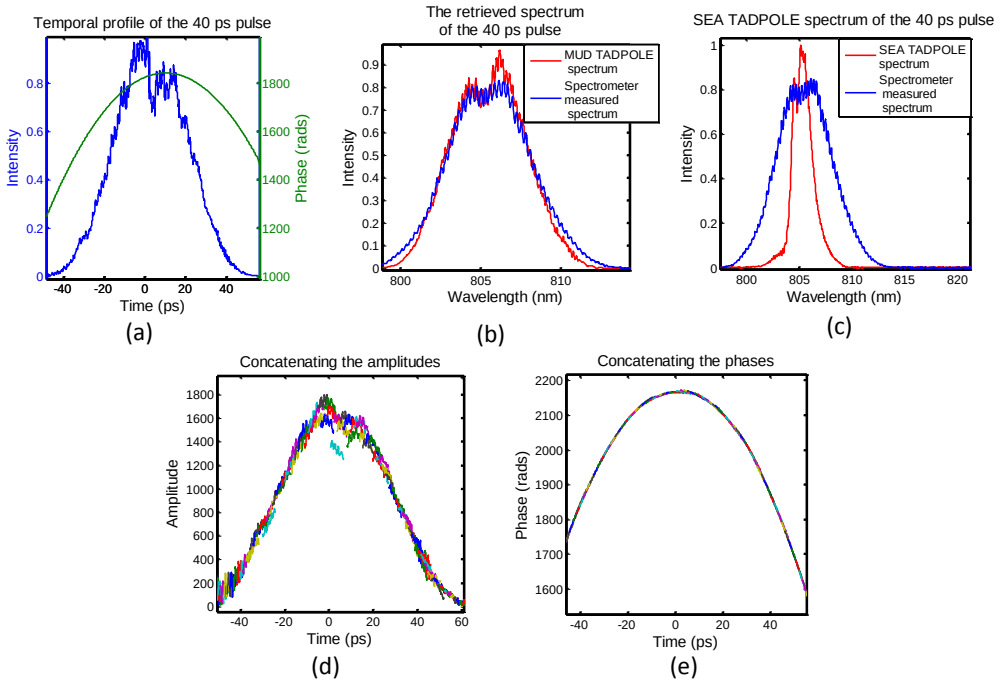

Fig. 4.4. a. The MUD TADPOLE-retrieved temporal amplitude and phase of a chirped 40 ps pulse. b. The MUD TADPOLE-retrieved spectrum compared to an independently measured spectrum using a spectrometer. c. The measured SEA TADPOLE spectrum compared to the independently measured spectrum. The overly narrow SEA TADPOLE spectrum shows the need for MUD TADPOLE. d. Concatenation of the retrieved temporal amplitudes, $A_i(t-\tau_i)$. Similar to Step 3 in Fig. 4.2, each color represents the retrieved amplitude at a different delay, which shows the multiple measurements overlapping in time as discussed in Section 4.3.3. e. Concatentation of the retrieved temporal phases after re-phasing, $\varphi_i(t-\tau_i)$.

Figure 4.4(c) highlights the limitations of SEA TADPOLE compared with MUD TADPOLE. It shows the spectrum measured by SEA TADPOLE and also by a spectrometer. It is clear that the spectrum retrieved from SEA TADPOLE is too narrow.

Since the 40 ps pulse was highly chirped, different colors occurred at different times in the pulse, and the reference pulse inside the spectrometer of SEA TADPOLE stretched only long enough to interfere with ~1.9 nm of the chirped-pulse spectrum. The other wavelengths are missing from the SEA TADPOLE spectral measurement. In contrast, Fig. 4.4(b) shows that MUD TADPOLE retrieves the entire 40 ps pulse.

Figure 4.4(d) and (e) show the concatenation of both the amplitude and phase used in Step 3 of the concatenation routine. As illustrated in Fig. 4.2, the amplitudes and phases were individually concatenated, and the different colors represent different measurements made with each individual SEA TADPOLE trace.

Our next experiment highlighted the large temporal range and high temporal resolution of MUD TADPOLE. Additionally, it also exposes the limitations of a conventional spectrometer. In this experiment we measured a chirped double pulse at multiple delays. At delays larger than 40 ps, the double pulse exhibited fine spectral-intensity features that were resolvable by MUD TADPOLE, but unresolvable by a conventional spectrometer.

The double pulse was generated by placing a Michelson interferometer after the single-grating pulse compressor. For this experiment we reduced the bandwidth of the incident pulse to 3.4 nm in order to fit the entire pulse within the temporal range of MUD TADPOLE, which is limited by the scanning range of our delay stage. As a result, we used a 300 mm focal length cylindrical lens inside the spectrometer to further spread out the reduced bandwidth on on the camera.

In contrast to the previous measurement shown in Fig. 4.4, the reduced bandwidth of the incident pulse on the compressor resulted in the stretching of the incident pulse to 22 ps FWHM.

Figure 4.5 shows both the measured and simulated temporal intensity and phase of two linearly chirped pulses at variable delays with respect to one another. Fig. 4.5 demonstrates a phenomena known as chirped pulse beating [44], which occurs because at each point in time the frequency content of each pulse differs by a constant beat frequency. This beat frequency is proportional to the delay, τ, between the two pulses.

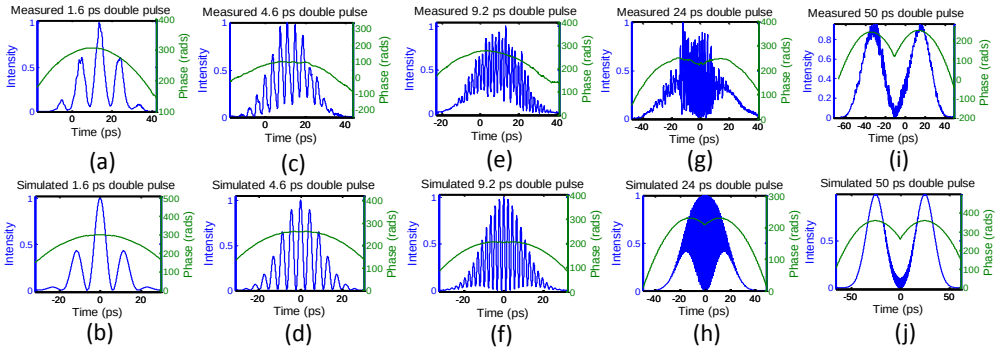

Fig. 4.5. A comparison of the measured and calculated temporal profiles of a chirped double pulse at variable delays. a,b. The MUD TADPOLE retrieved and simulated temporal profile of two 22 ps linearly chirped pulses separated by 1.6 ps. c,d. The retrieved and simulated temporal profile after increasing the delay between pulses to 4.6 ps. e,f. The retrieved and simulated temporal profile after increasing the delay between pulses to 9.2 ps. g,h. The retrieved and simulated temporal profile after increasing the delay between pulses to 24 ps. At this large delay the temporal phase develops a cusp which MUD TADPOLE is able to retrieve. i,j. The retrieved and simulated temporal profile of a 50 ps double pulse. At such a large delay the temporal beating is not as noticeable as at much shorter delays because fewer frequencies are temporally overlapped. In all examples the agreement between the retrieved and simulated results is good. These results simultaneously highlight the extended temporal range and high temporal resolution of MUD TADPOLE.

Figure 4.5 simultaneously highlights the high temporal resolution and the large temporal range of MUD TADPOLE. The temporal resolution of MUD TADPOLE is determined by the spectral range of the spectrometer used in Fig. 4.1. In this experiment our spectrometer had a spectral range of 30 nm and a temporal resolution of 71 fs. This high temporal resolution was put to good use in the measurement of the double pulse with a 24 ps delay shown in Fig. 4.5(g). The fast temporal beating which had a temporal period of 622 fs is well resolved by MUD TADPOLE.

A double pulse afforded us another opportunity to check the validity of our measurements. Using an optical power meter, the ratio of the intensities of the two pulses in the double pulse was found to be 0.99, or almost equal. MUD TADPOLE confirms this measurement as shown in Fig. 4.5(i), where the intensities of the retrieved fields are shown to be roughly equal.

Another interesting aspect to note is that MUD TADPOLE has the capability to measure pulses with phase cusps shown in Fig. 4.5(g) and (i).

Although the experimental and simulated results agree quite well, there is some disagreement, which is attributed to the slight instability of the Michelson interferometer used to make the double pulse. The use of an actively stabilized interferometer to make the double pulse would result in better agreement between our simulations and experimental results.

Figure 4.5(i) highlights the long temporal range of MUD TADPOLE, which is an equivalent measure of its spectral resolution. This fact is better explained by examining the spectrum corresponding to the 50 ps double pulse.

Figure 4.6(a) and (b) show both the retrieved temporal profile and the retrieved spectrum of the 50 ps double pulse. Since the two pulses are separated by such a large time delay, the spectral fringes are too fine for the high-resolution Ocean Optics spectrometer to resolve; the spectral fringes due to a double pulse measured by a spectrometer with .01 nm spectral resolution wash out completely at around 40 ps. In contrast, MUD TADPOLE resolves them accurately.

Apart from the spectral fringes, Fig. 4.6(b) shows that the envelope of the MUD TADPOLE-retrieved spectrum and that of the spectrometer measured spectrum agree, as they should.

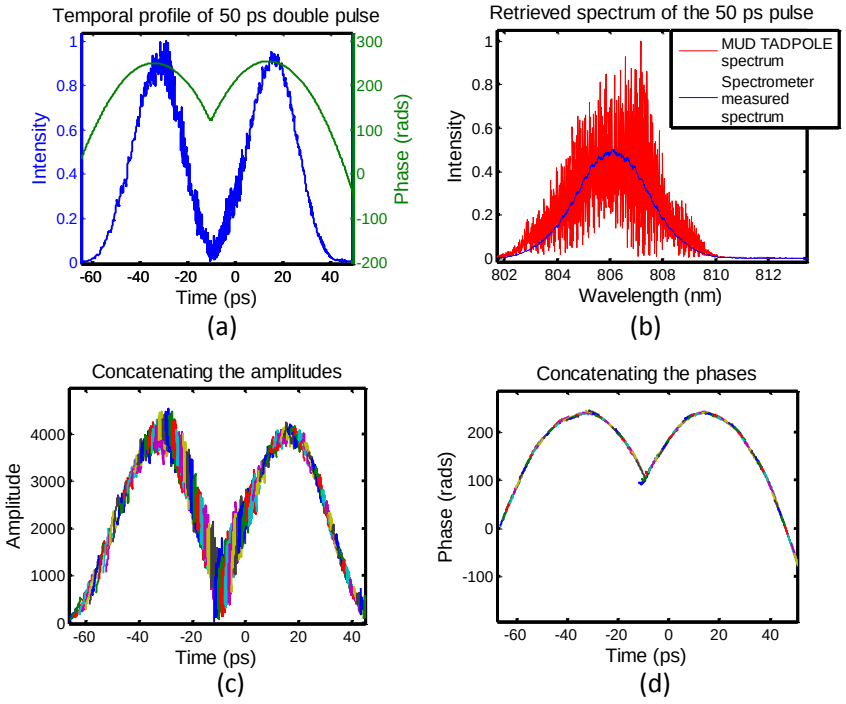

Fig. 4.6. a. The MUD TADPOLE-retrieved temporal intensity and phase of a 50 ps chirped double pulse. b. The retrieved spectrum compared to an independently measured spectrum. The spectrum shows the high spectral resolution of MUD TADPOLE, and it highlights a conventional spectrometer's limitions. c. Concatenation of the retrieved temporal amplitudes, $A_i(t-\tau_i)$. Similar to Step 3 in Fig. 4.2, each color represents the

retrieved amplitude at a different delay. e. Concatentation of the retrieved temporal phases after re-phasing, $\varphi_i(t-\tau_i)$.

Additionally, the measurement of the temporal phase of each of the pulses (shown in green in Fig. 4.6(a)) gives us more confidence in MUD TADPOLE. We expect the measured temporal chirp to be almost equal, given that both pulses were chirped equally by the single grating pulse compressor. Although the chirp of the two pulses is not exactly the same due to the geometry of a Michelson interferometer, where one pulse makes three passes through a partially reflecting 1 cm beam splitter, while the other pulse makes only a single pass, this amount of added chirp is negligible compared to that introduced by the pulse compressor.

Figure 4.6(c) and (d) show the concatenation of both the amplitude and phase used in Step 3 of the concatenation routine. As illustrated in Fig. 4.2, the amplitudes and phases were individually concatenated. Fig. 4.6(d) shows that the concatenation routine described in section 4.3.3 is able retrieve phases with cusps.

4.6 Summary and limitations

In summary we have used a variation of SEA TADPOLE that we call MUD TADPOLE to completely characterize pulses up to 100 ps in length with 71 fs resolution, achieving a length-to-resolution ratio of over 1400. MUD TADPOLE has successfully measured complex pulses with time-bandwidth products of ~700.

There is no fundamental limit to the length (or complexity) of a pulse that can be measured by MUD TADPOLE. Experimentally, the limit is given by the scanning range

of the delay stage in Fig. 4.1. This limit will also depend on the dynamic range of the camera, because for extremely long pulses, the fringes will not be visible in the presence of potentially more intense DC terms. As the unknown pulse duration increases, the fringe contrast for each measurement will decrease, because fringes only occur at times where the pulses temporally overlap (τ_{sp}), so most of the intensity will be in the DC. In the perfect case where the reference pulse temporally overlaps with the entire unknown pulse, the ratio between the signal term and the DC term will be 1/2. But if the unknown pulse duration is $1000\tau_{sp}$, the ratio between the DC and signal term will be 1/2000 requiring a dynamic range of more than 2000 (greater than 10 bits). In other words, a 10 bit camera (maximum of 1024 counts) could measure a pulse of maximum length $500\tau_{sp}$. For this latter case, for a pulse with a bandwidth of 5nm, and τ_{sp} = 10ps, the maximum TBP of a pulse that can be measured using MUD TADPOLE is ~ 70,000.

Additionally, there is no fundamental limitation to the spectral range, or equivalently, the temporal resolution of the device. Experimentally, the spectral range is limited by the camera size. By choosing a camera with a larger array size, MUD TADPOLE could accommodate larger bandwidths.

One fundamental limitation of MUD TADPOLE is that it is an interferometric method that requires a well-characterized reference pulse. Therefore, it can only measure pulses that are temporally and spectrally overlapped with the reference pulses. Furthermore, since MUD TADPOLE is a multi-shot method, it requires the unknown source to be stable over the entire scanning range of the delay stage. The experiments performed in this paper lasted about 15 minutes and consisted of 100 traces. This makes it ideal for measuring pulses modified by a time-stationary filter [16], such as a pulse

stretcher and/or compressor [13]. In contrast, pulses generated from phenomena with rapid variations from shot to shot, like continuum generation [45], may be difficult to measure accurately using MUD TADPOLE.

Additionally, an experimental limitation of MUD TADPOLE is imposed by the accuracy of the delay stage. The accuracy of the delay stage is important with regards to Step 2 of the MUD TADPOLE retrieval algorithm described in Section 4.3.2. In this step, each retrieved temporal electric field is temporally shifted from the reference pulse time frame to the lab frame. It is important that the accuracy of the time delay control (the delay stage in Fig. 4.1) be much less than the temporal resolution of MUD TADPOLE. Otherwise, each retrieved field will not be properly shifted resulting in discontinuities when concatenating.

The scanning stage used had an accuracy of 0.035μm corresponding to a delay accuracy of 0.12 fs. This is sufficient as it is much less than the temporal resolution of MUD TADPOLE which was 71 fs considering the spectral range of the spectrometer was 30 nm.

A modified version of the MUD TADPOLE retrieval algorithm could be applied to dual quadrature spectral interferometry [46] to increase its temporal range or equivalently its spectral resolution. The only modification in the setup would be an additional delay stage in the reference arm of the Mach-Zehnder interferometer to provide the variable delay.

In contrast, Fourier-transform spectral interferometry (FTSI) [5] could *not* be improved in this manner because a large delay is required between the reference and unknown pulses, and this cannot be scanned, because the Fourier retrieval algorithm

requires filtering along the spectral dimension. In contrast, MUD TADPOLE does not have this limitation, because its filtering is performed in the spatial domain.

In the future, we plan to implement MUD TADPOLE in a manner similar to [43] in order to measure the full spatio-temporal field of long complex pulses and also to modify it for single-shot measurements.

We believe that this simple, compact, and inexpensive device can measure pulses with time-bandwidth products in excess of 70,000 using inexpensive, off-the-shelf components. Also, it could improve the spectral resolution of any spectrometer by a large factor.

CHAPTER 5

MEASURING EXTREMELY COMPLEX ULTRASHORT PULSES USING MULTIPLE-DELAY CROSSED-BEAM SPECTRAL INTERFEROMETRY

5.1 Introduction

In the previous chapter we introduced MUD TADPOLE, a version of SI designed to measure very complicated pulses. In this chapter we demonstrate that MUD TADPOLE is capable of measuring pulses with TBPs exceeding 65,000. In other words, we show that MUD TADPOLE is capable of measuring pulses with higher temporal and spectral resolution than any other measurement technique. Yet, there are limits to the complexity of a pulse that MUD TADPOLE can measure.

In this chapter we first describe the limitations of MUD TADPOLE, and then show two examples of very complex measurements.

5.2 Time-bandwidth product limits of MUD TADPOLE

The maximum TBP that an ordinary spectrometer can measure is its finesse (its spectral range divided by its resolution). This is equal to the amount of information in the measured spectrum. At first glance, the maximum TBP that MUD TADPOLE can measure is the same quantity, but with the spectral resolution replaced by the inverse delay range, which would be MUD TADPOLE's finesse.

MUD TADPOLE's maximal TBP is, however, limited by another experimental factor: the dynamic range of the camera. This is because, as the reference pulse only

makes spatial fringes with the temporal piece of the unknown pulse with which it temporally overlaps, the rest of the unknown pulse also inevitably impinges on the camera, yielding a spatially structureless background of no value to that particular measurement and which must therefore be filtered out. While the relevant Fourier filtering works very well, this background could become very large for very complex pulses that are long compared to the spectrometer-broadened reference pulse. Thus, the dynamic range of the camera used in the spectrometer poses a limit to the largest TBP measurable by MUD TADPOLE. Fortunately, all that is necessary is to measure the phase of the spatial fringes against this background, and this can be done quite sensitively, even with as little as an oscillation amplitude of a fraction of a count, against a large constant background. Using one count as the limit, we may estimate that the largest TBP measurable by a MUD TADPOLE apparatus is the product of the finesse of the spectrometer and the dynamic range of the camera used to make the measurement. If the camera is chosen to match the spectrometer, that is, its number of columns is equal to the spectrometer finesse, then the maximal TBP measurable with MUD TADPOLE is the product of the number of columns (or rows, whichever is greater) and its dynamic range.

The best commercially available cameras, to our knowledge, have a dynamic range of 16 bits or ~64,000, and cameras have as many as a few thousand columns. Thus MUD TADPOLE should be able to measure pulses with a TBP as large as 10^8. For more complex pulses, clever methods for measuring oscillations of less than one count could improve its performance.

5.3 Data analysis

5.3.1 Spatial Fourier filtering

The first step in analyzing a MUD TADPOLE trace is spatial filtering [36, 40]. It is essentially a Fourier band-pass filter that isolates the spatial-fringe signal term from the, in principle, spatially structureless background. In practice, the background can vary slowly along the spatial direction due to beam spatial mode structure, which can cause some of the background to "leak into" the retrieved signal. This excess background in the signal term is not a problem when the spatial-fringe signal is relatively strong, as is the case for simple pulses. But for complex pulses, the background term can become a significant contribution. In our experiments, however, which use single-mode fibers for the input pulses, the spatial mode is quite flat, and this effect is not a problem.

5.3.2 Temporal filter

In practice, we find it preferable to actually use delays smaller than the length of the spectrometer-broadened reference pulse in order to avoid using the weak leading and trailing regions of the product of the reference pulse and the retrieved temporal piece of the pulse. So, after the retrieved spectra for the various delays are Fourier transformed to the "time" domain, retrieved pulse information at both large and small delays is discarded as clearly not part of the piece of the unknown pulse.

5.3.3 Constant background subtraction

We also perform constant background subtraction before temporally filtering the data. We subtracted a constant background from the retrieved MUD TADPOLE spectrogram (Fig. 5.1(a) and Fig. 5.2(a)), and we found that this significantly reduces the high frequency noise in the retrieved temporal amplitude and phase. In the experiments described in this paper, we simply subtracted the maximum noise value from the retrieved spectrogram and then set any negative points that resulted from the subtraction to zero.

Although this background subtraction ultimately reduces the dynamic range, we still obtained excellent agreement between the retrieved and expected results.

5.4 Experimental setup

We performed experiments using a KM Labs Ti:Sapphire oscillator. The pulses were centered at 800 nm, with a FWHM bandwidth of ~40 nm. Using a Swamp Optics GRENOUILLE 8-20USB [47], the input pulse was measured to have a temporal width of 285fs. The pulses were stretched to a FWHM length of 70 ps using a grating pulse compressor.

The SEA TADPOLE set-up shown in Fig. 4.1 is described in more detail in [36]. Specifically, for our set-up we used a 100 mm focal-length spherical lens to collimate and cross the beams emanating from the fibers. Additionally, a 600 grooves/mm grating and 100 mm focal-length lens were used for mapping wavelength to position in the spectrometer. The delay stage used was a Newport M-IMS600CC Linear Stage with a

Newport ESP300 single-axis controller. The total scanning range of the delay stage was 120cm which provided MUD TADPOLE's high spectral resolution.

We did not perform any experiments that were limited by the dynamic range of the camera due to the difficulty in generating such a complex pulse. We know of only a few simple methods to increase the TBP of a pulse. The temporal length of the pulse can be increased through the use of a fiber, pulse shaper/stretcher/compressor, or etalon. Or, the spectral bandwidth of the pulse can be increased by a nonlinear optical process like self-phase-modulation. In our experiment the limited pulse energies, 5nJ per pulse with a repetition rate of 85 MHz, prevented us from significantly increasing the TBP by a nonlinear optical process.

Additionally, generating a complex pulse with a fiber is impractical. For example, to stretch a 50nm pulse up to 3ns yielding a TBP of ~70,000 requires 170m of standard fused silica fiber. Using more dispersive fiber reduces the path length but increases the cost significantly. Furthermore, to stretch the pulse an equivalent amount using a standard grating compressor would require 70m of path length. Both methods prove experimentally challenging for any optical setup and especially so for SI, which requires equivalent path lengths for both the reference and unknown pulses.

The final method for stretching a pulse uses an etalon or Michelson interferometer which "stretches" the incident pulse by generating multiple replicas. This method results in a relatively simple temporal structure compared with the other methods, but the resulting spectrum is highly oscillatory and hence interesting.

Even better, the use of a combination of a pulse compressor and an etalon to generate a train of highly chirped pulses proved to be the best solution—and a good test

of our method. The compressor used was a grating compressor with a path length of 2m which stretched the incident pulse from 285fs up to ~70ps FWHM. The etalon consisted of two partially reflecting mirrors with a 90% reflecting coating. The high reflectivity of the two mirrors was chosen to minimize the relative intensity difference of the pulses in the pulse train.

5.5 Results and discussion

We performed two experiments to demonstrate MUD TADPOLE's unique capabilities compared to other pulse characterization techniques. In both experiments MUD TADPOLE provides the necessary spectral resolution to completely characterize the intensity and phase of the unknown pulse.

In the first experiment, we measured a double pulse consisting of two linearly chirped pulses stretched to 70ps FWHM. Over the entire 120cm scanning range, 2800 SEA TADPOLE traces were used, each having a different reference-pulse delay using the set-up shown in Fig. 4.1.

The spectrometer used in this setup had half the spectral resolution and twice the spectral range of the previous MUD TADPOLE setup [35]. As a result the reference pulse stretches in time from 285fs to $\tau_{sp} \sim 4$ps inside the spectrometer. The reference pulses were separated in time by $\tau_{ref} = 1.46$ps. Since $\tau_{ref} < \tau_{sp}$ there was sufficient overlap with neighboring reference pulses, which minimized discontinuities during the concatenation routine. The half width at 1/e of the weighting function [35] was chosen to be equal to the temporal separation of the reference pulses, $\tau_G = 1.4$ ps.

Figure 5.1(a) shows the retrieved MUD TADPOLE spectrogram. The spectrogram is an intuitive representation of the individual SEA TADPOLE measurements at many delays and is easily computed from them. The slope of the lines in the spectrogram indicates that each pulse in the train is heavily chirped. A quick glance at the spectrogram shows that each line has the same slope indicating that each pulse has an identical chirp value. This is expected because, before the Michelson interferometer, which served to make the double pulse, the pulse was chirped by the pulse compressor. This is confirmed by Fig. 5.1(b) which shows the MUD TADPOLE retrieved temporal profile of the pulse, in which the temporal phase of each pulse is almost identical.

Figure 5.1(b) displays the retrieved temporal profile of the chirped double pulse. The ratio of the measured intensities of each pulse in the double pulse was 0.6. Using a power meter, the ratio of the intensities of the two pulses in the double pulse was found to be 0.8. This discrepancy is likely due to misalignment of the Michelson interferometer, yielding better coupling of one pulse than the other into the optical fiber.

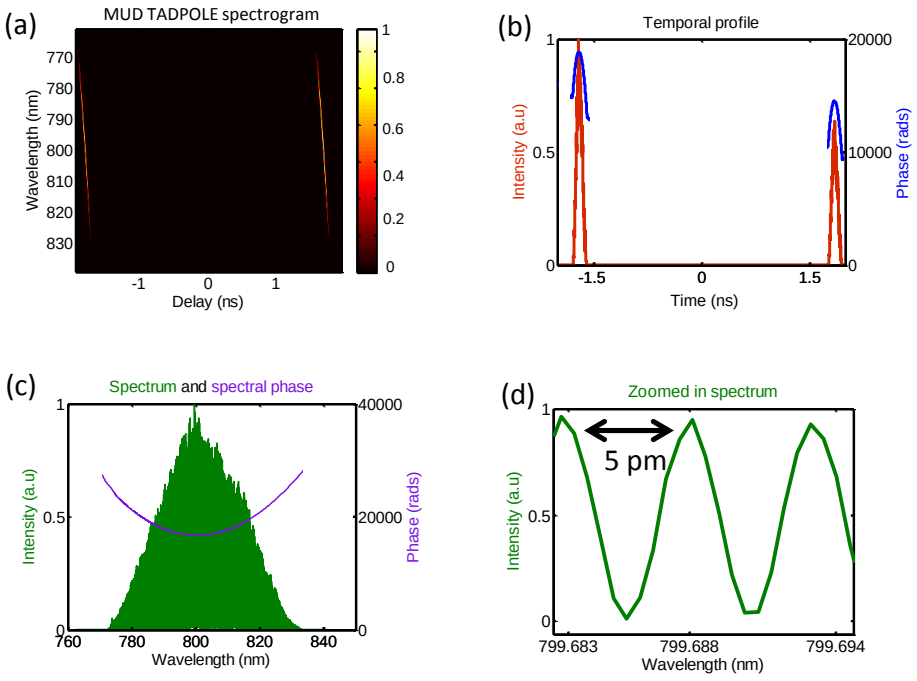

Fig. 5.1. a. The MUD TADPOLE spectrogram of a 3.5 ns chirped double pulse. b. The retrieved temporal intensity and phase of a 3.5 ns pulse. c. The MUD TADPOLE-retrieved spectrum. The solid color of the spectrum is due to the massive fine spectral structure in the complex pulse, which MUD TADPOLE is able to resolve. d. A zoomed in plot of a small section of the spectrum demonstrates MUD TADPOLE's high spectral resolution. The periodicity of the fringes in the spectrum was 5 pm.

Figure 5.1(c) highlights the high spectral resolution of MUD TADPOLE. The fringes are so fine that there is not sufficient spatial resolution on the page to reveal them all. Figure 5.1(d) shows an enlarged region of the spectrum, which illustrates that the fringe spacing is 5 pm. Such fine features in the spectrum have until now only been measurable with a very high resolution etalon spectrometer.

Our next experiment highlighted MUD TADPOLE's dynamic range and ability to measure even more complicated pulses. In this experiment we measured a train of chirped pulses.

The train of pulses was generated by placing a mirror pair, each with a 90% partially reflecting face, after the single-grating pulse compressor. The mirrors were not precisely parallel, but still yielded a train of pulses at their output. As in the previous experiment, each pulse in the pulse train had a FWHM temporal width of 70ps and a FWHM spectral bandwidth of 40nm.

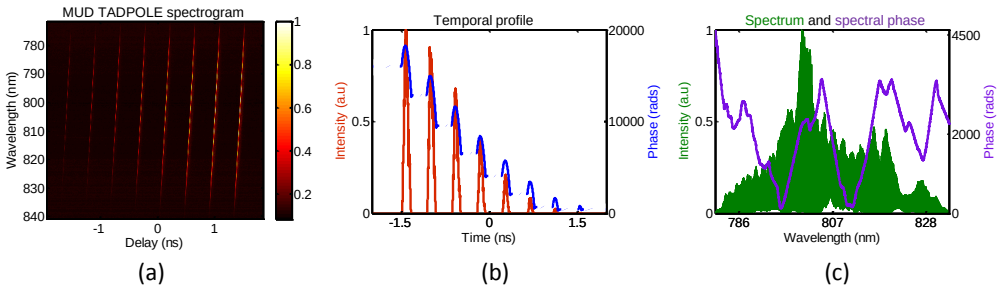

Fig. 5.2 a. The MUD TADPOLE spectrogram of a train of linearly chirped pulses. b. The temporal profile of the train of pulses. The measurement shows the steadily decreasing intensities of the pulses, the expected result of the multiple relections inside the etalon. c. The spectrum of the pulse train. As expected, the asymmetric spectrum results from the nonparallel mirror pair and the differing absolute phases of the individual pulses in the pulse train. A more detailed view of the complex spectrum is shown in Media 1, which is a movie that scans the spectrum along the entire spectral domain.

Figure 5.2(a) shows the retrieved MUD TADPOLE spectrogram. As in the previous figure, the slope of the lines in the spectrogram indicates that each pulse in the train is heavily chirped. This is expected because, before the mirror pair that generated the pulse train, the pulse was chirped by the pulse compressor. This is confirmed by Fig. 5.2(b), which shows the MUD TADPOLE retrieved temporal profile of the pulse.

The measured intensities of the pulses in the pulse train decrease in time, as expected. Although the temporal profile of the measurement in Fig. 5.2(b) is relatively simple, the spectral profile is complex, and MUD TADPOLE should be capable of

measuring pulses with even more complex temporal profiles because it has proven capable of measuring pulses with 622 fs substructure [35].

Figure 5.2(c) shows the retrieved spectrum of the pulse train, which exhibits MUD TADPOLE's large spectral range, ~50nm in this measurement. A striking feature of the spectrum is its complex shape. In contrast to the spectrum of a chirped double pulse (Fig. 5.1(c)), which has a Gaussian envelope, the spectrum shown in Fig. 5.2(c) is more complex. The unique shape is attributed to two factors. First, the two partially reflecting mirrors were deliberately aligned not to be parallel, in order to avoid back reflections back into the laser. This slight misalignment results in a different temporal spacing between the adjacent pulses in the pulse train, which corresponds to different spectral-fringe periodicities in the spectral domain. This is in contrast to the measurement of the double pulse in which there is only one periodicity in the spectral fringes due to the single temporal spacing between the two pulses. Second, the absolute phase of each individual pulse in the pulse train differed, which shifted the spectral fringes due to each pulse in the train of pulses, and which served to further distort the envelope of the spectrum.

An instructive way to view the complex spectral structure in Fig. 5.2(c) is by scanning the spectrum along the wavelength axis. Figure 5.2(c)(Media 1) is a movie that simultaneously highlights MUD TADPOLE's high spectral resolution and large spectral range. The movie shows the complex spectral structure that can result from a seemingly noncomplex pulse in time, Fig. 5.2(b).

There is a noticeable discrepancy between the maximum TBP MUD TADPOLE can measure and that reported in this paper. The TBP for both MUD TADPOLE

measurements (Fig. 5.1-2) was ~65,000, in reasonable agreement with the maximum TBP for the 3000 x 2208, 8-bit CMOS camera used in this experiment of about 10^6. Our setup was actually limited by the range of delay, rather than dynamic range of the camera, and the same experimental setup could have measured a much more complicated pulse, had we generated it.

5.6 Conclusion

We have demonstrated the first general technique for the measurement of complex pulses with TBP exceeding 65,000 with fs temporal resolution, ns temporal range, pm spectral resolution, and nm spectral range. We believe that this simple and inexpensive device can be used to accurately characterize seed pulses used in chirped pulse amplification (CPA) systems and arbitrary optical waveforms with TBPs as large as 10^8. Indeed, the parameters of our device fairly closely match that required to measure an arbitrary optical waveform from a Ti:Sapphire oscillator with a pulse separation of several ns and should allow measurements of extremely complex waveforms in general.

CHAPTER 6

SINGLE-SHOT MULTIPLE DELAY CROSSED BEAM SPECTRAL INTERFEROMETRY

6.1 Introduction

In Chapters 4 and 5 we introduced MUD TADPOLE, a variation of SI capable of measuring very complex pulses. Yet, MUD TADPOLE is a multi-shot method, and therefore it requires the unknown source to be stable over the entire scanning range of the delay stage. As a result, it is unable to measure transient optical phenomena that vary from shot to shot.

In this chapter we introduce a single-shot version of MUD TADPOLE for measuring such transient phenomena. It is to our knowledge the first single-shot technique for measuring complex waveforms that temporally interleaves hundreds of measurements with sub-ps temporal resolution. Here we first review MUD TADPOLE and explain the modifications required for a single-shot version.

MUD TADPOLE is a simple temporal scanning version of SEA TADPOLE [36], another variation of SI that involves crossing at an angle the pulse to be measured with a previously measured reference pulse. The crossed beams generate a *spatial* interferogram, from which the unknown pulse's intensity and phase can be *spatially* filtered without loss of spectral resolution. Additionally, SEA TADPOLE employs fibers as inputs for both the reference and unknown pulse which greatly reduces the alignment burden commonly associated with SI.

It is these two simple yet powerful features of SEA TADPOLE, (1) the filtering is done along the spatial dimension rather than the spectral dimension and (2) the use of fibers as conduits to the imaging spectrometer, which result in the very high spectral resolution of MUD TADPOLE. As a direct consequence of these two features, the interference between the reference pulse and the unknown pulse at any delay (assuming they are temporally overlapped to some degree) will result in the same spatial fringe periodicity, thereby ensuring that the spatial resolution required to filter the signal is the same regardless of delay. This allows for a temporal scanning SI measurement, something which is not possible in standard Fourier transform SI (FTSI). In FTSI a large delay is required between the reference and unknown pulse, and an increase in the delay further increases the spectral resolution required for accurate retrieval.

We exploit this unique characteristic of SEA TADPOLE in the form of MUD TADPOLE, which makes multiple SEA TADPOLE measurements at multiple delays, scanning the reference pulse along the typically much longer unknown pulse in time. Due to the limited spectral resolution of the spectrometer used, each SEA TADPOLE measurement yields a measurement of the electric field of a section of the unknown pulse equal to the reciprocal of the spectral resolution of the spectrometer. After the entire length of the unknown pulse has been scanned, the multiple delayed SEA TADPOLE measurements are temporally interleaved, or concatenated, to construct the full temporal electric field of the unknown pulse.

To modify MUD TADPOLE to the single-shot regime, a multitude of delayed SEA TADPOLE measurements must be made in a single-shot. We accomplish this by crossing the unknown pulse with a reference pulse with pulse-front tilt (PFT) generating

a spatial interferogram similar to that obtained in SEA TADPOLE. Except here no fibers are required for the conduits of the two pulses, because the reference pulse is not scanned in time and the alignment burden is not as high as in a collinear interferometry setup.

The tilted pulse front of the reference pulse provides a linear transverse time delay along the spatial dimension of an imaging spectrometer (see Fig. 6.1). The result is *N* SEA TADPOLE measurements of the electric field of the unknown pulse, each delayed in time by an amount proportional to the PFT, η. Provided that the range of delay generated, the product of the PFT and the spatial range of the imaging spectrometer, is greater than or equal to the temporal length of the unknown pulse, τ_{unk}, or $\eta \cdot \Delta x_c \geq \tau_{unk}$, then the full temporal electric field of the unknown pulse can be reconstructed by temporally interleaving the *N* linearly delayed measurements.

Using PFT to increase the range of delay to measure pulses has been well-documented in the literature [48-49]. Additionally, we recently used a very similar crossed-beam SI method to measure the spatio-temporal field of a pulse with a PFT angle of 89.9° and a delay range of several ns [50]. Yet, to our knowledge there has been no demonstration using PFT to temporally interleave the resulting measurement.

In this chapter we theoretically model single-shot MUD TADPOLE, detail the limitations with regards to complex pulse measurement, and show proof-of-principle results.

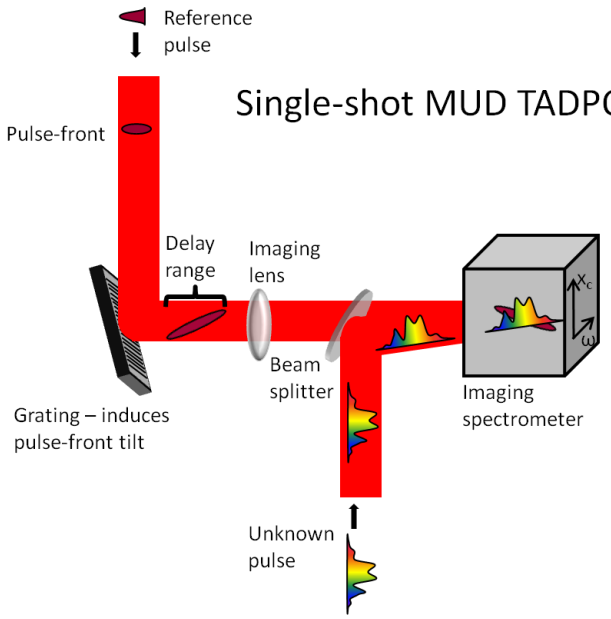

Fig. 6.1 Experimental setup for single-shot MUD TADPOLE. The pulse-front of the spatially uniform reference pulse is tilted along the horizontal dimension by a grating. The imaging lens images the plane of the grating onto the detector of the imaging spectrometer ensuring that the only spatio-temporal coupling in the reference pulse is PFT. The unknown pulse is incident on the imaging spectrometer at a slight angle, θ, with respect to the reference pulse. This crossing of the two pulses results in a spatial interferogram with spatial fringes along the x_c dimension at the detector of the imaging spectrometer.

6.2 Single-shot MUD TADPOLE Theory

The single-shot MUD TADPOLE retrieval algorithm consists of three steps, a spatial Fourier-filtering step, a temporal Fourier filtering step, and temporal concatenation. Although the single-shot MUD TADPOLE retrieval algorithm is very similar to that of multi-shot MUD TADPOLE [35] there are a few differences, and for that reason a detailed explanation is necessary.

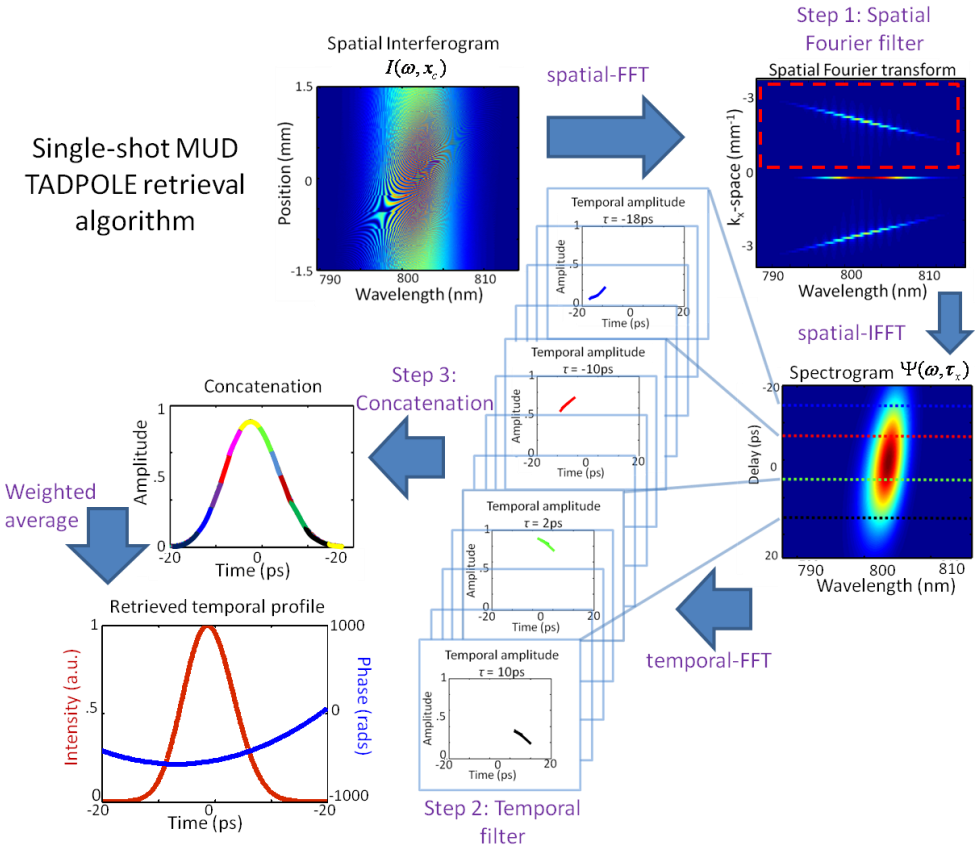

Fig. 6.2 The single-shot MUD TADPOLE retrieval algorithm of a chirped pulse. In Step 1, the MUD TADPOLE trace is spatially Fourier filtered. First the interferogram is spatially Fourier transformed along the x_c-axis. Then the signal term is filtered and shifted in k_x-space, and inverse Fourier transformed back to the spatial domain. The amplitude and phase of the reference pulse are divided out of each row of the resulting field spectrogram. Each row of the spectrogram corresponds to the electric field of the unknown pulse at a different delay, $\Psi(\omega, \tau_x)$. In Step 2, the

retrieved fields are temporally filtered keeping only the region in which the unknown and reference pulse are temporally overlapped. Each retrieved field, $\Psi(\omega, \tau_x)$, is Fourier transformed to the time domain and temporally shifted to the lab frame yielding $\tilde{\Psi}_{lab}(t-\tau_x)$. In the figure, each color represents the retrieved field at a different delay. Although, only the amplitudes are shown, after re-phasing the same process is done with the retrieved phases. In Step 3, the retrieved amplitude and phase are separately concatenated using a weighted average, resulting in the retrieved temporal profile of the entire unknown pulse.

6.2.1 Step 1: spatial Fourier filter

Single-shot MUD TADPOLE uses crossed beam SI to generate the signal trace. In crossed beam SI the electric field of the unknown pulse is retrieved from a spectrally resolved spatial interferogram resulting from the crossing of two beams. The interferogram is given by the following equation

$$I(\omega, x_c) = |E_u(\omega, x_c) + E_r(\omega, x_c)|^2, \tag{6.1}$$

where $E_u(\omega,x_c)$ and $E_r(\omega,x_c)$ are the electric fields of the unknown and reference pulse, respectively, and x_c is the spatial coordinate along the crossing dimension. Since the unknown beam is spatially uniform over the camera detector, the electric field of the unknown pulse can be written in the form

$$E_u(\omega, x_c) = A_u(\omega - \omega_0)e^{i(\varphi_u(\omega-\omega_0)+kx_c\sin\theta)}, \tag{6.2}$$

where $A_u(\omega - \omega_0)$ and $\varphi_u(\omega - \omega_0)$ are the amplitude and phase of the unknown pulse, ω_0 is the center frequency, k is the wavenumber, and θ is the crossing angle of the unknown beam.

Similarly, we can model the spatio-temporal field of the reference pulse with PFT. To do so, we start in the (t, x_c) domain. In this domain the electric field of the reference pulse is given by

$$E_r(t, x_c) = E_{r_t}(t - \eta x_c) E_{r_x}(x_c), \tag{6.3}$$

where η is the PFT imparted by the grating. In Eq. (6.3) we have assumed that apart from PFT, $E_r(t, x_c)$ has no additional spatio-temporal couplings of its coordinates. In other words, the reference pulse incident upon the diffraction grating must be spatially smooth with no spatio-temporal distortions. Additionally, we make use of the paraxial approximation resulting in $\eta = \sin\theta_d \approx \lambda_0/d$ with θ_d being the diffracted angle from the grating, λ_0 being the center wavelength, and d being the groove spacing of the grating. Taking a Fourier transform of Eq. (6.3) along the time-domain yields

$$E_r(\omega, x_c) = E_{r_\omega}(\omega - \omega_0) E_{r_x}(x_c) e^{i\eta(\omega-\omega_0)x_c}. \tag{6.4}$$

Next, re-writing Eq. (6.4) in terms of the spectral amplitude, phase, and crossing angle yields

$$E_r(\omega, x_c) = A_r(\omega - \omega_0) e^{i(\varphi_r(\omega-\omega_0) - kx_c \sin\theta + \eta(\omega-\omega_0)x_c)}, \tag{6.5}$$

where $A_r(\omega - \omega_0)$ and $\varphi_r(\omega - \omega_0)$ are the amplitude and phase of the reference pulse.

Plugging in Eq. (6.2) and (6.5) into Eq. (6.1) yields the intensity measured by the imaging spectrometer

$$\begin{aligned} I(\omega, x_c) \;=\; & |A_u(\omega-\omega_0)|^2 + |A_r(\omega-\omega_0)|^2 + \\ & 2A_r(\omega-\omega_0)A_u(\omega-\omega_0)\cos\left[i\left(\Delta\varphi(\omega-\omega_0) + 2kx_c\theta + \eta(\omega-\omega_0)x_c\right)\right], \end{aligned} \tag{6.6}$$

where $\Delta\varphi(\omega - \omega_0)$ is the spectral phase difference between the reference and unknown pulse, c is the speed of light in vacuum, and we have used the small-angle approximation for the crossing angle, θ.

We use a Fourier retrieval algorithm to filter the signal term from the interferogram. To do this we first take a spatial Fourier transform of Eq. (6.6)

$$\tilde{I}(\omega,k_x)=\left(|A_u(\omega-\omega_0)|^2+|A_r(\omega-\omega_0)|^2\right)\delta(k_x)+\ldots$$
$$2A_r(\omega-\omega_0)A_u(\omega-\omega_0)e^{\pm i\Delta\varphi(\omega-\omega_0)}\delta\left(k_x\pm\left[2\frac{\omega}{c}\theta+\eta(\omega-\omega_0)\right]\right). \tag{6.7}$$

Eq. (6.7) shows that the result of the spatial Fourier transform is three terms. The DC background is located at $k_x = 0$, and the signal term, which contains both the amplitude and phase of the unknown pulse, is off-center. The k_x-value of the signal term is determined by the crossing angle, θ, and the PFT, η, of the reference pulse.

In the filtering routine we isolate the signal term and shift it to the $k_x = 0$ value, which is equivalent to adding a constant, $-2\omega_0\theta/c$, inside the delta function of the third term in Eq. (6.7). Therefore, after filtering and shifting, the retrieved signal term is

$$\tilde{I}_{retrieved}(\omega,k_x)=A_r(\omega-\omega_0)A_u(\omega-\omega_0)e^{\pm i\Delta\varphi(\omega-\omega_0)}\delta\left(k_x\pm\left[\left(2\frac{\theta}{c}+\eta\right)(\omega-\omega_0)\right]\right). \tag{6.8}$$

This term is then inverse Fourier transformed along the spatial domain and the amplitude and phase of the reference pulse are divided out yielding

$$\Psi(\omega,x_c)=A_u(\omega-\omega_0)e^{i\left[\varphi_u(\omega-\omega_0)+\left(2\frac{\theta}{c}+\eta\right)(\omega-\omega_0)x_c\right]}. \tag{6.9}$$

Eq. (6.9) is the retrieved field spectrogram shown in Fig. 6.2. By grouping different variables, we can rewrite Eq. (6.9) in a clearer fashion. First, we set

$$E(\omega-\omega_0)=A_u(\omega-\omega_0)e^{i\varphi_u(\omega-\omega_0)}. \tag{6.10}$$

This term is the electric field of the unknown pulse. Next, we set

$$\tau_x=\left(2\theta/c+\eta\right)x_c, \tag{6.11}$$

because the PFT maps position to delay. Substituting Eq. (6.10) and (6.11) into Eq. (6.9) yields

$$\Psi(\omega,\tau_x)=E(\omega-\omega_0)e^{i(\omega-\omega_0)\tau_x}. \tag{6.12}$$

Taking a 1-D Fourier transform of Eq. (6.12) along the spectral dimension yields

$$\tilde{\Psi}(t,\tau_x) = \tilde{E}(t+\tau_x)e^{i\omega_0 t}. \tag{6.13}$$

Equations (6.12) and (6.13) show that each row of the field spectrogram is the retrieved electric field, $\Psi_{(\omega,\tau_x)}$, at a different delay, τ_x. Additionally Eq. (6.11) shows that τ_x varies linearly along the filtered spatial dimension of the imaging spectrometer. Therefore, a simple test pulse can be used to calibrate the delay axis, τ_x. For example, the experiments described in this paper used a double pulse of a known temporal separation for calibrating the delay axis.

6.2.2 Step 2: temporal Fourier filter

Since Eq. (6.13) shows that the use of a reference pulse with pulse-front-tilt provides both (1) a range of delays and (2) *linearly* maps delay to position on the imaging spectrometer, we can reconstruct the entire unknown pulse in time by temporally interleaving the linearly delayed measurements given by Eq. (6.13). But before temporally interleaving, each delayed measurement must be temporally filtered because each section of the reference pulse only measures a small temporal range of the unknown pulse.

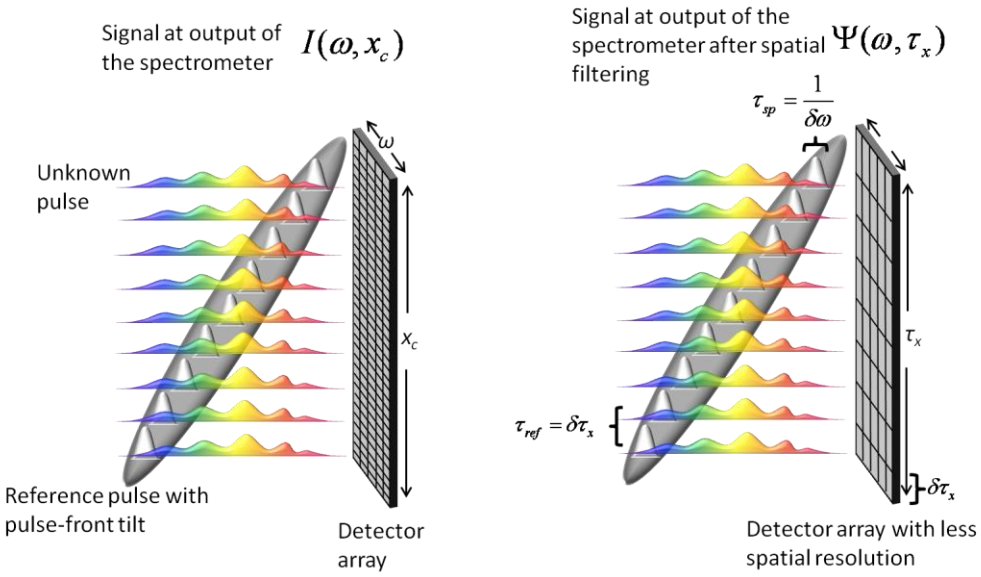

Fig. 6.3 The gating of the unknown pulse with the tilted reference pulse at the output of the spectrometer before and after spatial filtering. The spatial distribution of the unknown pulse is uniform over the entire detector, whereas the reference pulse exhibits PFT. The single-shot MUD TADPOLE trace, $I(\omega,x_c)$ is spatially filtered yielding the field spectrogram, $\Psi(\omega,\tau_x)$. The spatial filtering effectively reduces the number of delayed spectral measurements. Additionally, due to the finite spectral resolution of the imaging spectrometer, each spectral measurement made by the detector can only measure a section of the unknown pulse equal to the inverse of its spectral resolution, $\tau_{sp} = 1/\delta\omega$. Yet, the temporal length of the reference pulse on each row of the detector, τ_{ref}, is equal to the resolution of the delay axis, $\delta\tau_x$. Therefore, to ensure an accurate measurement of each section of the unknown pulse $\tau_{ref} < \tau_{sp}$.

Temporal filtering is performed because each section of the reference pulse interferes with a section of the unknown pulse of length τ_{sp} (see Fig. 6.3), which is smaller than the time-axis of the retrieved pulse, and only information within this region is kept while that from larger and smaller times is discarded (see step 2 Temporal filter in Fig. 6.2).

In this step, the spectrogram is first Fourier transformed along the spectral dimension to the time domain i.e.

$$\Psi(\omega,\tau_x) \Rightarrow \tilde{\Psi}(t,\tau_x). \tag{6.14}$$

Next, we crop each field such that:

$$\tilde{\Psi}(t,\tau_x) = \begin{cases} \tilde{\Psi}(t,\tau_x) \text{ for } \tau_x - \dfrac{\tau_{sp}}{2} < t < \tau_x + \dfrac{\tau_{sp}}{2} \\ 0 \text{ otherwise} \end{cases} . \tag{6.15}$$

After temporally filtering, each retrieved electric field is shifted in time because each measurement is time averaged over the frame rate of the detector. In other words, the field retrieved at the delay τ_x on the detector, $\tilde{\Psi}(t,\tau_x)$, is centered around $t = 0$, the local zero time value of that measurement.

In order to concatenate the individual measurements, the retrieved fields must be transformed from the local time frame of each τ_x to the lab frame in which all of the spectral measurements occur at different times. This means that the retrieved field, $\tilde{\Psi}(t,\tau_x)$, is linearly shifted by τ_x,

$$\tilde{\Psi}(t,\tau_x) \Rightarrow \tilde{\Psi}_{lab}(t-\tau_x) . \tag{6.16}$$

6.2.3 Step 3: concatenation

After temporally filtering and shifting the retrieved fields to the lab frame, we can retrieve the full electric field of the unknown pulse by temporal interleaving or concatenating the sampled electric fields.

Due to the spectrometer's finite spectral resolution, the accuracy of each individual measurement at τ_x decreases away from the temporal origin. To account for this we use a weighted averaging scheme which weights each individual measurement

accordingly. Our weighting function is a Gaussian weighting function with a half width at 1/e, τ_G, which is less than τ_{sp} and centered on τ_x

$$G_x(t-\tau_x) = \exp\left[-\left(\frac{t-\tau_x}{\tau_G}\right)^2\right]. \tag{6.17}$$

The weighting function was chosen to be a Gaussian function because the temporal response function is approximately Gaussian in form [39, 41] (see Fig. 6.4(a)).

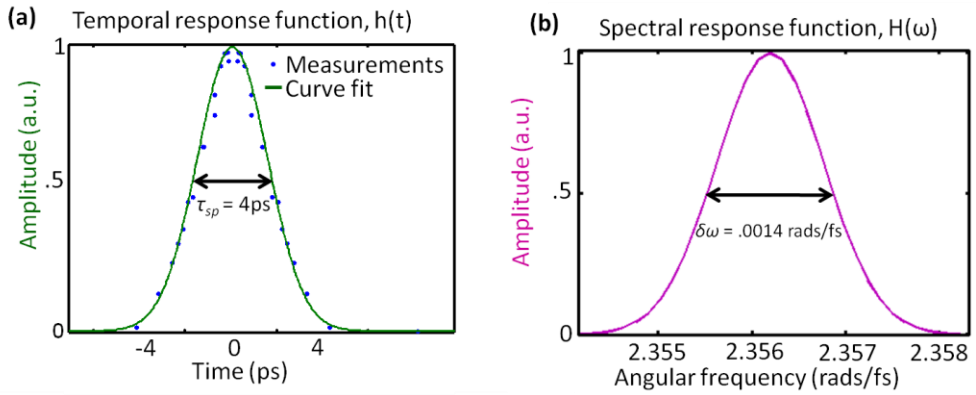

Fig. 6.4. a. The temporal response function, $h(t)$, of the imaging spectrometer used in the experiments in this paper. We measured the response function (dots) using a Michelson interferometer which generated a double pulse at varying delays. The solid curve is a fit to this data. b. The Fourier transform of $h(t)$, which is the spectral response function, $H(\omega)$. Note that we only measured $h(t)$ on one side of the time axis because we expect it to be a symmetric function because $H(\omega)$ is a real function. The measured FWHM of the temporal response function, τ_{sp}, was 4ps. Therefore, the imaging spectrometer can only accurately measure the spectrum of pulses with lengths < 4ps, or equivalently, pulses with spectral features $\delta\omega$ > .0014 rads/fs (or $\delta\lambda$ = .05nm).

The accuracy of the experimental results are unaffected by variation of the width of the Gaussian weighting function as long as the width is less than τ_{sp}, and greater than or equal to the delay spacing, τ_{ref}, or,

$$\tau_{ref} \leq \tau_G < \tau_{sp}. \tag{6.18}$$

Additionally, to obtain a better retrieval and reduce discontinuities when concatenating, we average together multiple delayed measurements. This is possible because the delay between successive measurements, τ_{ref}, is less than τ_{sp}. Therefore, a given section of the unknown pulse is reliably retrieved by more than one measurement. Therefore, we average together this redundant information to obtain a better retrieval.

Finally, the retrieved fields are concatenated together. We do this by separating each $\tilde{\Psi}_{lab}(t-\tau_x)$ into its constituent phase and amplitude,

$$\tilde{\Psi}_{lab}(t-\tau_x) = A_x(t-\tau_x)e^{i\varphi_x(t-\tau_x)}. \tag{6.19}$$

Similar to the original MUD TADPOLE technique [35], in which the absolute phase of each individual measurement was re-phased, we perform the same re-phasing to reduce discontinuities in the retrieved phase when concatenating. This can be done easily because the temporal sections of the unknown pulse measured by subsequent reference pulses overlap. Therefore, the absolute phase of two individual measurements of the same time are set equal.

Next, both the phases, $\varphi_x(t-\tau_x)$, and amplitudes $A_x(t-\tau_x)$, are separately superposed using a weighted average, yielding the entire temporal amplitude and phase of the unknown pulse:

$$A_{final}(t) = \frac{\sum_{j=1}^{N} G_j(t-\tau_j)A_j(t-\tau_j)}{\sum_{i=1}^{N} G_i(t-\tau_i)}, \tag{6.20}$$

$$\varphi_{final}(t) = \frac{\sum_{j=1}^{N} G_j(t-\tau_j)\varphi_j(t-\tau_j)}{\sum_{i=1}^{N} G_i(t-\tau_i)}. \tag{6.21}$$

The product of the amplitude and phase yields the entire temporal amplitude and phase of the unknown pulse

$$\tilde{E}_{final}(t) = A_{final}(t)e^{i\varphi_{final}(t)}. \tag{6.22}$$

Figure 6.2 graphically represents the single-shot MUD TADPOLE retrieval algorithm.

6.3 Limitations on pulse-front-tilt, temporal range, and TBP

Although single-shot MUD TADPOLE has the unique property that it is not limited by the spectral resolution of the spectrometer, its spectral resolution cannot be increased without limit. Increasing the spectral resolution requires increasing the PFT of the reference pulse. Since PFT is a spatio-temporal coupling, a larger value will result in finer spatial fringes in the spatial interferogram. Finer spatial fringes will have a reduced contrast due to the limited spatial resolution of the imaging spectrometer. Therefore, both the crossing angle and the PFT which show up in the parameter τ_x in Eq. (6.11) must be chosen small enough so that the spatial resolution does not wash the fringes out entirely, and large enough so that the signal term can be extracted from the Fourier transform of the interferogram.

In this section we detail the limitations of single-shot MUD TADPOLE. First, we discuss how the PFT must be matched to the spectral resolution of the spectrometer. Next, we derive the maximum PFT that can be used for single-shot MUD TADPOLE. Lastly, we derive the maximum TBP measurable.

6.3.1 Matching PFT to the spectral resolution of the spectrometer

The amount of PFT that can be used is determined by the limited *spectral* resolution of the imaging spectrometer. In single-shot MUD TADPOLE, an imaging spectrometer will make N measurements of the unknown pulse at N different delays. Fig. 6.3 illustrates the interference of the unknown pulse and the tilted reference pulse at the output of the imaging spectrometer.

Due to the spectrometer's finite spectral resolution, it can only measure a section of the unknown pulse up to the inverse of its spectral resolution, $\tau_{sp} = 1/\delta\omega$. Yet, the temporal length of the reference pulse at a given delay is, τ_{ref}. Therefore, to ensure an accurate measurement of each section of the unknown pulse, the condition $\tau_{ref} < \tau_{sp}$ must be satisfied. If this condition is not met (because the PFT of the reference pulse is too large ($\tau_{ref} > \tau_{sp}$)) each spectral measurement will lack the appropriate spectral resolution to resolve those features of the unknown which are finer than the spectral resolution.

6.3.2 Matching the PFT to the spatial resolution of the imaging spectrometer

Not only must the PFT be matched to the spectral resolution, but it must also be matched to the *spatial* resolution of the imaging spectrometer. In order to extract the signal term from the Fourier transform of the interferogram, it must be well-separated from the DC background in k_x-space. Eq. (6.7) shows the equation for the Fourier transform of the interferogram. The third term contains the signal and is therefore the term of interest. This term is a line in k_x-space (see Fig. 6.5) that is governed by the equation

$$k_x(\omega) = 2\frac{\omega}{c}\theta + \eta(\omega - \omega_0). \tag{6.23}$$

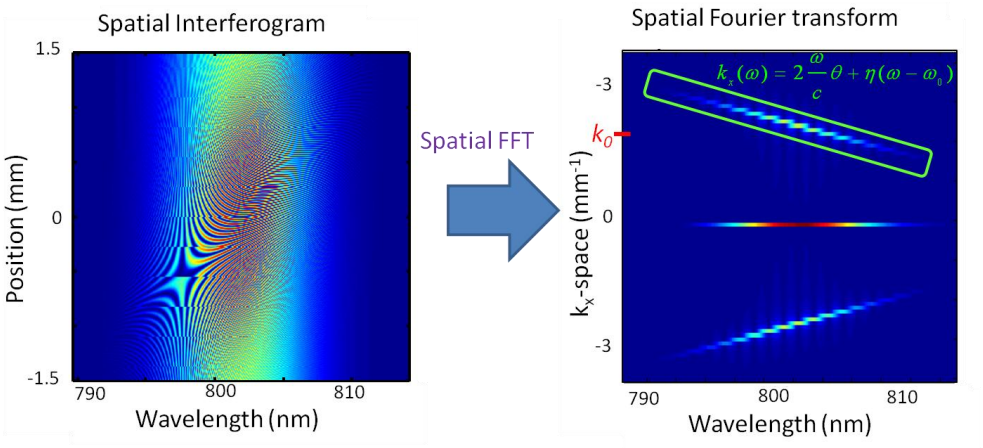

Fig. 6.5. The interferogram and the spatial Fourier transform of the interferogram. The green rectangle highlights the linear slope of the signal in k_x-space, and the equation governing the line is given by Eq. (6.23). Here k_0 is the center of the signal distribution in k_x-space.

To avoid aliasing and properly filter the signal term from the DC term, the condition that $k_x > 0$ must be satisfied. Using this constraint, and the fact that the above equation is smallest when $\omega = \omega_{min}$, we can solve for the maximum value of the PFT for a given crossing angle.

$$0 < 2\frac{\omega_{\min}}{c}\theta + \eta(\omega_{\min} - \omega_0). \tag{6.24}$$

Using the relation $\omega_{min} = \omega_0 - \Delta\omega/2$ and rearranging Eq. (6.24) to solve for the PFT

$$\eta < \frac{4\theta(\omega_0 - \Delta\omega/2)}{\Delta\omega c}. \tag{6.25}$$

For the maximum PFT, the inequality in Eq. (6.25) becomes an equality.

To allow for the maximum value of PFT, the center of the signal distribution given by Eq. (6.23) will be located in the center of the upper half of the Fourier transformed image shown in Fig. 6.5 or

$$k_0 = \frac{\pi}{2\delta x_c}, \tag{6.26}$$

where, δx_c is the pixel width. Using Eq. (6.23, 6.26) we can solve for the crossing angle of the center frequency

$$\theta_0 = \frac{c\pi}{4\delta x \omega_0}. \tag{6.27}$$

Plugging in numbers, λ_0 = 800nm and a pixel width of 3.5μm, δx = 3.5μm, into Eq. (6.27) yields a crossing angle of ~1°.

Using Eq. (6.25, 6.27) we can solve for the maximum amount of PFT which can be used to measure a pulse with single-shot MUD TADPOLE

$$\eta_{\max} = \frac{\pi}{\delta x_c \omega_0}\left(\frac{\omega_0}{\Delta\omega} - \frac{1}{2}\right). \tag{6.28}$$

A spectral range of ~20nm, center wavelength of ~800nm, and a pixel size of 3.5 μm, yields a value for the maximum possible PFT as η_{max} = .015 fs/nm.

The temporal range is given by the product of the PFT and the spatial extent of the imaging spectrometer

$$\Delta t = \eta \cdot \Delta x_c = \eta \cdot N_x \cdot \delta x_c. \tag{6.29}$$

where N_x is the number of points along the spatial dimension of the imaging spectrometer.

Using Eq. (6.28, 6.29) the maximum temporal range can be calculated

$$\Delta t = \frac{\pi N_x}{\omega_0}\left(\frac{\omega_0}{\Delta\omega} - \frac{1}{2}\right). \tag{6.30}$$

For the experimental parameters used in this paper, a spectral range of ~20nm, center wavelength of ~800nm, a pixel size of 3.5 μm, and a camera with 3000 pixels in the spatial dimension yields a maximum temporal range of Δt = 158 ps.

6.3.3 TBP limitations

Now that we have found the maximum PFT, we can solve for the maximum TBP measurable by single-shot MUD TADPOLE.

Using Eq. (6.30) the maximum TBP is

$$TBP = \Delta t \Delta f = \frac{N_x \pi}{2}\left(1 - \frac{\Delta\omega}{2\omega_0}\right). \tag{6.31}$$

Using the experimental parameters used in this paper, the maximum TBP is ~4,500. It is worth noting that the maximum TBP which MUD TADPOLE can measure is proportional to the number of pixels along the spatial dimension. Therefore, if we used a custom rectangular 6 megapixel detector array (30,000 x 200), and kept the spectral range constant, then the maximum TBP would be 45,000 which corresponds to a 20nm pulse centered around 800nm that has been stretched to ~5ns in length.

6.4 Experimental setup

We performed experiments using a Coherent MIRA Ti:Sapphire oscillator. The pulses were centered at 809 nm, with a FWHM bandwidth of 4 nm, at a repetition rate of 76MHz, and had pulse energies of ~5.2nJ per pulse.

A simplified version of the single-shot MUD TADPOLE experimental set-up is illustrated in Fig. 6.1. The reference pulse is incident upon a 10.5cm x 10.5cm 1200 groove/mm grating at near grazing incidence, ~89° with respect to the grating normal.

The near-grazing incidence caused the reference beam to fill the entire 10.5cm grating which maximized the amount of PFT induced along the horizontal dimension.

The pulse at the surface of the grating was imaged by a two lens imaging system that also de-magnified the beam by a factor 2.5. The reason for de-magnifying the beam was to increase the PFT of the reference pulse, thereby increasing the range of delay by a factor equal to the de-magnification, 2.5. The first lens in the imaging system was located a focal length, f_1 = 85cm, away from the grating. The second lens with a focal length, f_2 = 35cm, was located a distance, $f_1 + f_2$ = 120cm, from the first lens and a distance f_2 = 35cm away from the detector of the imaging spectrometer. The two lens imaging system imaged the plane of the grating onto the detector of the imaging spectrometer which ensured that the only spatio-temporal coupling in the reference pulse was PFT.

A periscope was used to rotate the reference pulse out of the plane such that the PFT occurred in the vertical dimension. This was done because the imaging spectrometer spectrally resolved the beam along the horizontal dimension.

The imaging spectrometer consisted of a 600 groove/mm grating and a 100cm focal length cylindrical lens. A CMOS detector with 3000 x 2208 pixels collected the image. The imaging spectrometer used in this setup had a spectral resolution of $\delta\lambda$ = .05nm/pixel ($\delta\omega$ = .0014 rads/fs/pixel). We measured the temporal response function (see Fig. 6.4(a)) of the spectrometer by measuring the spectral fringe contrast due to two temporally overlapped pulses at varying delays [18, 50]. The FWHM of the temporal response function was experimentally determined to be τ_{sp} = 4ps. Additionally, each spectral measurement was separated in time by τ_{ref} = 200 fs. Since $\tau_{ref} < \tau_{sp}$ there was

sufficient overlap with neighboring reference pulses which reduced discontinuities during the concatenation routine.

Additionally, the temporal resolution of single-shot MUD TADPOLE is determined from the spectral range which in this experiment was 17nm, resulting in a temporal resolution of 125fs.

The half width at 1/e of the weighting function [35] was chosen to be equal to the temporal separation of the reference pulses, τ_G = 200fs, thereby satisfying the condition that $\tau_{ref} \leq \tau_G < \tau_{sp}$ [35].

Lastly, we performed two different image processing methods to reduce the effects of noise on the retrieved images. There are a number of methods which can be employed to limit the degrading effects of noise. In the first two sets of data (see Fig. 6.6, 6.8), our signal was stable enough to allow for frame summing, which helped reduce the effect of noise. In the third experiment (see Fig. 6.9), in place of frame summing, we employed a median filter [51] which served to reduce the "salt and pepper" noise. We found this to be more effective than frame summing while still preserving the single-shot nature of the technique.

6.5 Results and discussion

We performed three experiments to demonstrate single-shot MUD TADPOLE's large temporal range/high spectral resolution. These experiments demonstrate how single-shot MUD TADPOLE dramatically improves the spectral resolution of the imaging spectrometer. In each experiment, single-shot MUD TADPOLE provides the necessary

spectral resolution to completely characterize the intensity and phase of the unknown pulse.

Fig. 6.6 shows the single-shot MUD TADPOLE measurement of a train of 9 pulses separated by ~4ps. The train of pulses was generated using an etalon composed of two partially reflecting mirrors with a reflectivity value of 90%. After the etalon, the pulse train was coupled into a 35cm fiber optic cable to chirp the pulse.

Fig. 6.6(a) shows the single-shot MUD TADPOLE trace. The spatial fringes (the signal term) generated from the interference between the unknown and the reference pulse are barely visible. This is because on each row of the detector the reference pulse only makes spatial fringes with the temporal piece of the unknown pulse with which it temporally overlaps. And, the rest of the unknown pulse also inevitably impinges on the camera (see Fig. 6.3), yielding a spatially structureless background of no value to that particular measurement and which must therefore be filtered out. This background is filtered out by performing a spatial Fourier transform (see Fig. 6.6(b)). The image of the Fourier transform of the trace clearly shows the signal term.

After the signal term is filtered and shifted in k_x-space, it is inverse Fourier transformed back to the spatial domain, and the amplitude of the reference pulse is divided out. We did not divide out the phase of the reference pulse from the spectrogram because the reference and unknown were derived from the same source. As a result, the measured phase difference was equal to that of the unknown pulse.

The field spectrogram is shown in Fig. 6.6(c). Here we have transformed the spatial dimension to delay, because the PFT of the reference pulse linearly maps position

to delay on the camera. The calibration of the delay axis was determined using a double pulse of a known temporal spacing.

The tilt of the spectrogram in Fig. 6.6(c) is due to the chirp of pulses in the pulse train which is expected because the pulse train was chirped by a 35cm fiber. The temporal fringes in the spectrogram are due to the temporal overlap of the neighboring pulses.

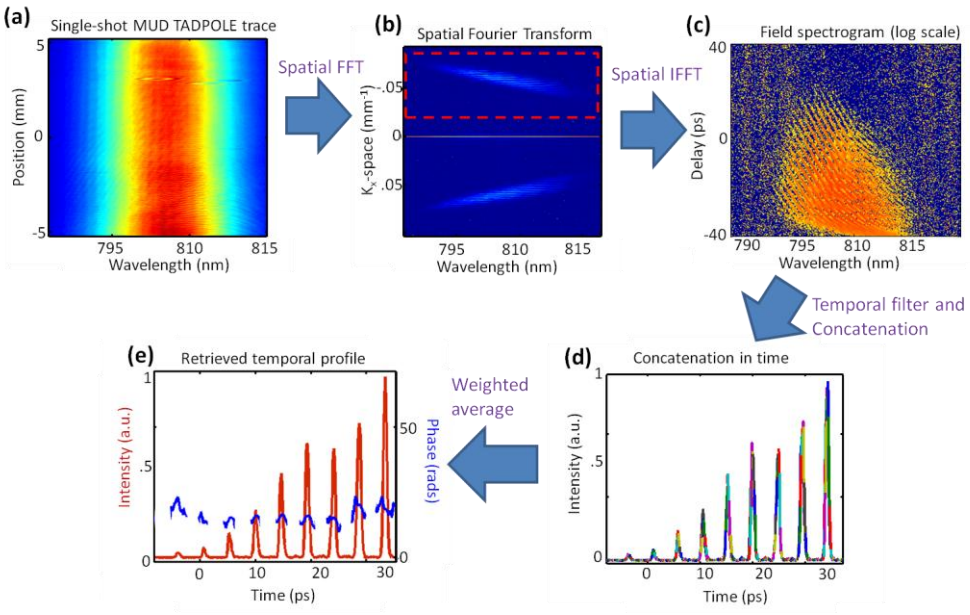

Fig. 6.6. Single-shot MUD TADPOLE measurement of a 35ps pulse train. a. The single-shot MUD TADPOLE trace. b. The spatial Fourier transform of the trace. Here the signal term is filtered in k_x-space and inverse Fourier transformed back to the spatial domain. c. The field spectrogram, where we have tranformed the spatial axis to the delay axis because of the PFT of the reference pulse. d. The concatenation step of the MUD TADPOLE retrieval algorithm to concatenate the retrieved sections of the unknown pulse in time. Here each color represents the retrieved temporal electric field at a different delay. Although not shown, after re-phasing the the same concatenation scheme is performed with the temporal phase. e. After performing a weighted average over all the retrieved sections of the unknown pulse's amplitude and phase, the full temporal electric field of the unknown pulse is retrieved.

Next, the spectrogram is Fourier transformed along the spectral dimension to the "time" domain, and temporally filtered keeping only the region in which the unknown and that section of the reference pulse which are temporally overlapped. Fig. 6.6(d) shows how the delayed sections of the unknown pulse are then concatenated in time. Using the weighted averaging scheme described in Section 6.2.3, the delayed retrieved sections of the pulse are averaged together resulting in the full temporal profile of the unknown pulse (see Fig. 6.6(e)).

Fig. 6.6(e) shows that the pulse train had a length of ~35ps which is ~9 times larger than the FWHM of the temporal response function, τ_{sp}, of the spectrometer used (see Fig. 6.4(a)). Accordingly, the single-shot MUD TADPOLE technique increased the temporal range/spectral resolution of the imaging spectrometer by a factor of 9. Therefore, had we not used the single-shot MUD TADPOLE technique, the imaging spectrometer would only be capable of accurately measuring one of the 9 pulses in the pulse train.

Fig. 6.7 shows a zoomed in section of Fig. 6.6(d) of the fourth pulse in the pulse train located at the time value t = 18ps. The zoomed in picture highlights the smooth concatenation of the different sections of the unknown pulse. It demonstrates to our knowledge the first example of single-shot "temporal interleaving" with ~fs temporal resolution.

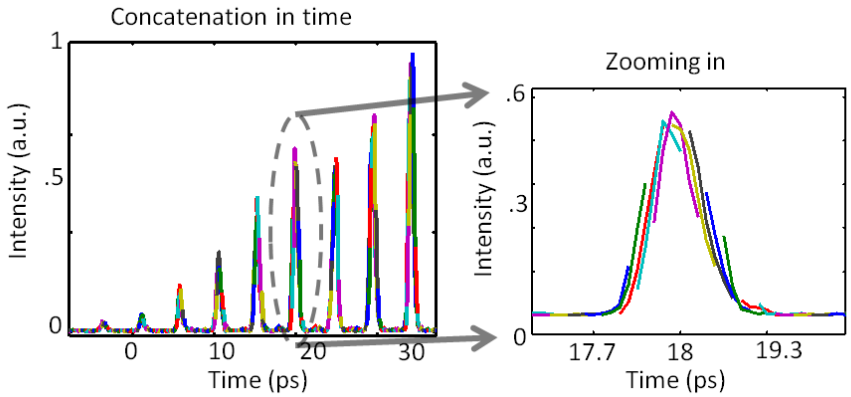

Fig. 6.7. A zoomed in view of the concatenation of the delayed measurements of the unknown pulse. The zoomed in figure exhibits the high accuracy to which the unknown pulse is concatenated. This figure shows to our knowledge the first example of single-shot "temporal interleaving" with fs temporal resolution. It should be noted that each retrieved section of the pulse does not line up perfectly. We attribute this to the small variations of the spatial intensity mask of the reference pulse. This effect is minimized by averaging together mulitple delayed measurements, therby reducing the discontinuities when concatenating.

Next we measured a 60ps pulse train (see Fig. 6.8) that was almost equal to the entire temporal range of single-shot MUD TADPOLE (~70ps). This measurement highlighted the relatively long temporal range of single-shot MUD TADPOLE.

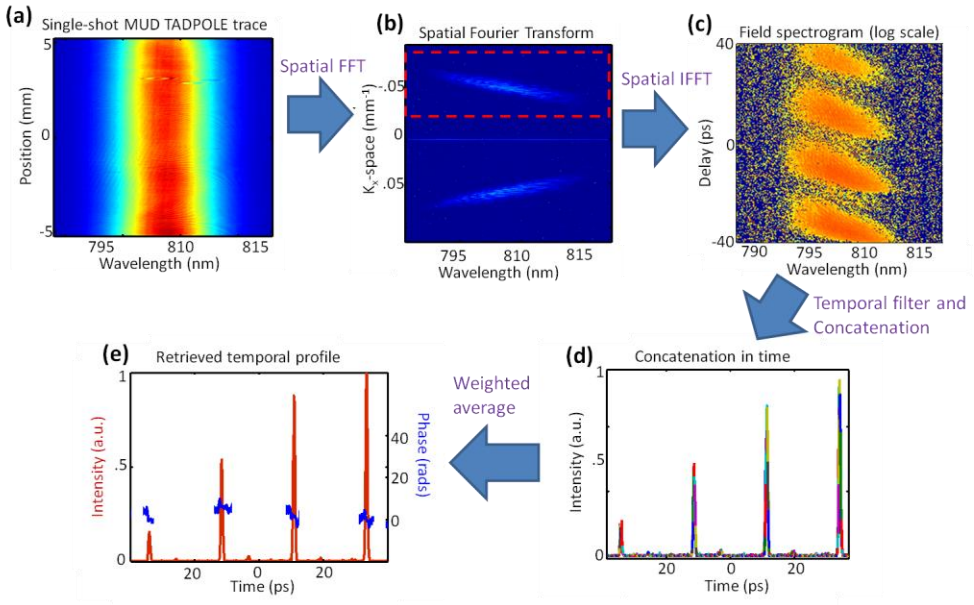

Fig. 6.8. Single-shot MUD TADPOLE measurement of a 60ps pulse train. a. The single-shot MUD TADPOLE trace. b. The spatial Fourier transform of the trace. Here the signal term is filtered in k_x-space and inverse Fourier transformed back to the spatial domain. c. The field spectrogram, where we have tranformed the spatial axis to the delay axis because of the PFT of the reference pulse. d. Using the concatenation step of the MUD TADPOLE retrieval algorithm to concatenate the retrieved sections of the unknown pulse in time. Here each color represents the retrieved temporal electric field in time at a different delay. Although not shown, the same concatenation scheme is performed with the temporal phase. e. After performing a weighted average over all the retrieved sections of the unknown pulse's amplitude and phase, the full temporal electric field of the unknown pulse is retrieved.

Although there is not much noticeable difference between the MUD TADPOLE trace and the spatial Fourier transform shown in both sets of data (Fig. 6.6, 6.8), the field spectrogram shown in Fig. 6.8(c) is noticeably different from that of Fig. 6.6(c). The reason for this is that the pulses in the pulse train are spaced 5 times further than in Fig. 6.6(c), ~20ps. Therefore, neighboring pulses in the pulse train are not temporally overlapped and no interference fringes result. Additionally, the field spectrogram clearly

shows a tilt for each pulse in the pulse train resulting from the chirp introduced by the 35cm fiber.

Fig. 6.8(e) shows that the pulse train had a length of ~60ps which is 15 times larger than the FWHM of the temporal response function, τ_{sp}, of the spectrometer used (see Fig. 6.4(a)). Accordingly, the single-shot MUD TADPOLE technique increased the temporal range/spectral resolution of the imaging spectrometer by a factor of 15.

Our next experiment highlighted the high temporal resolution of MUD TADPOLE. In this experiment we measured a chirped double pulse at multiple delays.

The double pulse was generated by an etalon composed of two partially reflecting mirrors with a reflectivity value of ~50%. After the etalon we chirped the pulses with a single-grating pulse compressor [52].

Figure 6.9 shows both the measured and simulated temporal intensity and phase of two linearly chirped pulses at variable delays with respect to one another. Fig. 6.9 demonstrates a phenomena known as chirped pulse beating [44], which occurs because at each point in time the frequency content of each pulse differs by a constant beat frequency. This beat frequency is proportional to the delay, τ, between the two pulses.

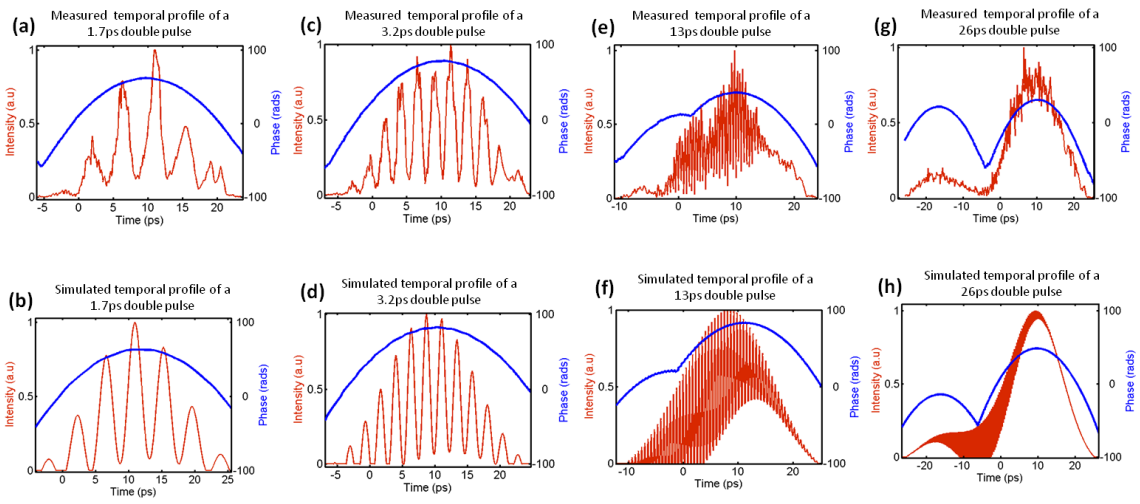

Fig. 6.9. A comparison of the measured and calculated temporal profiles of a chirped double pulse at variable delays. a,b. The MUD TADPOLE retrieved and simulated temporal profile of two 14 ps linearly chirped pulses separated by 3.7ps. c,d. The retrieved and simulated temporal profile after increasing the delay between pulses to 5ps. e,f. The retrieved and simulated temporal profile after increasing the delay between pulses to 13ps. At this large delay the temporal phase develops a cusp which MUD TADPOLE is able to retrieve. g,h. The retrieved and simulated temporal profile after increasing the delay between pulses to 25ps. At such a large delay the temporal beating is not as noticeable as at much shorter delays because fewer frequencies are temporally overlapped. In all examples the agreement between the retrieved and simulated results is good.

Figure 6.9 simultaneously highlights the high temporal resolution and the large temporal range of MUD TADPOLE. The temporal resolution of MUD TADPOLE is determined by the spectral range of the spectrometer used in Fig. 6.1. In this experiment our spectrometer had a spectral range of 17 nm and a temporal resolution of 125 fs. This high temporal resolution was put to good use in the measurement of the double pulse with a 13 ps delay shown in Fig. 6.9(e). The fast temporal beating which had a temporal period of 510 fs is well resolved by MUD TADPOLE.

Another interesting aspect to note is that MUD TADPOLE has the capability to measure pulses with phase cusps shown in Fig. 6.9(e) and (g).

6.6 Summary and limitations

We have introduced the first single-shot ultrashort pulse measurement technique that temporally interleaves hundreds of measurements with ~ 125fs temporal resolution. The experiments described above resulted in an increase in the spectral resolution of the spectrometer used by a factor of 15. Furthermore, we have used it to measure pulses up to 60ps with TBPs up to 112.

Although the demonstrated temporal range was ~70ps (about half the maximum value for the experimental parameters), the temporal range/spectral resolution of single-shot MUD TAPDOLE can be increased by either increasing the pulse front-tilt or using a larger detector array. The PFT can be increased by using a grating or etalon with larger PFT or de-magnifying the image of the reference pulse on the grating by a larger amount.

It must be noted that increasing the PFT (or equivalently the angular dispersion) to too large a value will make the paraxial approximation invalid (see Eq. 6.3-4). The result of this is that the transverse time delay of the reference pulse front will be nonlinear, and the delay between individual spectral measurements would not be constant. This effect can be easily calibrated using a simple test pulse.

Additionally the temporal range and hence complexity of pulse that can be measured cannot be increased without limit due to the finite spatial resolution of the imaging spectrometer. For a single-shot MUD TADPOLE using a few-megapixel camera and a low resolution spectrometer with 20 nm spectral range, the maximum TBP

that can be measured is ~4,500. Therefore, we believe that this simple and inexpensive device can be used to accurately characterize seed pulses used in CPA systems and provide the foundation for the measurement of arbitrary waveforms.

REFERENCES

1. R. Trebino, *Frequency-Resolved Optical Gating: The Measurement of Ultrashort Laser Pulses* (Kluwer Academic Publishers, Boston, 2002).

2. Y. Mairesse and F. Quere, "Frequency-resolved optical gating for complete reconstruction of attosecond bursts," Physical Review A **71**, 011401 (2005).

3. C. Iaconis and I. A. Walmsley, "Spectral phase interferometry for direct electric-field reconstruction of ultrashort optical pulses," Opt. Lett. **23**, 792-794 (1998).

4. J. R. Birge, R. Ell, and F. X. Kärtner, "Two-dimensional spectral shearing interferometry for few-cycle pulse characterization," Opt. Lett. **31**, 2063-2065 (2006).

5. C. Froehly, A. Lacourt, and J. C. Vienot, "Time impulse response and time frequency response of optical pupils," Nouvelle Revue D'Optique **4**, 183-196 (1973).

6. Z. Jiang, C.-B. Huang, D. E. Leaird, and A. M. Weiner, "Optical arbitrary waveform processing of more than 100 spectral comb lines," Nat Photon **1**, 463-467 (2007).

7. V. R. Supradeepa, C. M. Long, D. E. Leaird, and A. M. Weiner, "Self-referenced characterization of optical frequency combs and arbitrary waveforms using a simple, linear, zero-delay implementation of spectral shearing interferometry," Opt. Express **18**, 18171-18179 (2010).

8. N. K. Fontaine, R. P. Scott, L. Zhou, F. M. Soares, J. P. Heritage, and S. J. B. Yoo, "Real-time full-field arbitrary optical waveform measurement," Nat Photon **4**, 248-254.

9. M. H. Asghari, Y. Park, and J. Azaña, "Complex-field measurement of ultrafast dynamic optical waveforms based on real-time spectral interferometry," Opt. Express **18**, 16526-16538 (2010).

10. V. R. Supradeepa, D. E. Leaird, and A. M. Weiner, "Single shot amplitude and phase characterization of optical arbitrary waveforms," Optics Express **17**, 14433-14443 (2009).

11. M. A. Foster, S. Salem, D. F. Geraghty, A. Turner-Foster, M. Lipson, and A. L. Gaeta, "Silicon-chip-based ultrafast optical oscilloscope," Nature **456**, 81-84 (2008).

12. D. H. Broaddus, M. A. Foster, O. Kuzucu, A. C. Turner-Foster, K. W. Koch, M. Lipson, and A. L. Gaeta, "Temporal-imaging system with simple external-clock triggering," Opt. Express **18**, 14262-14269 (2010).

13. V. Chauhan, P. Bowlan, J. Cohen, and R. Trebino, "Single-diffraction-grating and grism pulse compressors," J. Opt. Soc. Am. B **27**, 619-624.

14. X. Gu, L. Xu, M. Kimmel, E. Zeek, P. O'Shea, A. P. Shreenath, R. Trebino, and R. S. Windeler, "Frequency-resolved optical gating and single-shot spectral measurements reveal fine structure in microstructure-fiber continuum," Opt. Lett. **27**, 1174-1176 (2002).

15. S. Linden, H. Giessen, and J. Kuhl, "XFROG-a new method for amplitude and phase characterization of weak ultrashort pulses," Physica Status Solidi B Conference Title: Phys. Status Solidi B (Germany) **206**, 119-124 (1998).

16. C. Dorrer and I. Kang, "Linear self-referencing techniques for short-optical-pulse characterization," J. Opt. Soc. Am. B **25**, A1-A12 (2008).

17. D. N. Fittinghoff, J. L. Bowie, J. N. Sweetser, R. T. Jennings, M. A. Krumbüugel, K. W. DeLong, R. Trebino, and I. A. Walmsley, "Measurement of the intensity and phase of ultraweak, ultrashort laser pulses," Opt. Lett. **21**, 884-886 (1996).

18. C. Dorrer, N. Belabas, J.-P. Likforman, and M. Joffre, "Spectral resolution and sampling issues in Fourier-transform spectral interferometry," J. Opt. Soc. Am. B **17**, 1795-1802 (2000).

19. L. Lepetit, G. Cheriaux, and M. Joffre, "Linear techniques of phase measurement by femtosecond spectral interferometry for applications in spectroscopy," J. Opt. Soc. Am. B **12**, 2467-2474 (1995).

20. P. O'Shea, M. Kimmel, X. Gu, and R. Trebino, "Highly simplified device for ultrashort-pulse measurement," Opt. Lett. **26**, 932-934 (2001).

21. J. Cohen, D. Lee, V. Chauhan, P. Vaughan, and R. Trebino, "Highly simplified device for measuring the intensity and phase of picosecond pulses," Opt. Express **18**, 17484-17497 (2010).

22. C. Radzewicz, P. Wasylczyk, and J. S. Krasinski, "A poor man's FROG," Optics Communications **186**, 329-333 (2000).

23. S. Akturk, M. Kimmel, P. O'Shea, and R. Trebino, "Extremely simple device for measuring 20-fs pulses," Opt. Lett. **29**, 1025-1027 (2004).

24. S. Akturk, M. Kimmel, and R. Trebino, "Extremely simple device for measuring 1.5-µm ultrashort laser pulses," Opt. Express **12**, 4483-4489 (2004).

25. S. Akturk, M. Kimmel, P. O'Shea, and R. Trebino, "Measuring pulse-front tilt in ultrashort pulses using GRENOUILLE," Opt. Express **11**, 491-501 (2003).

26. D. Lee and R. Trebino, "Extremely simple device for measuring ultrashort pulses in the visible," in *Lasers and Electro-Optics, 2009 and 2009 Conference on Quantum electronics and Laser Science Conference. CLEO/QELS 2009. Conference on*, 2009), 1-2.

27. D. Lee, Z. Wang, X. Gu, and R. Trebino, "The effect--and removal--of an ultrashort pulse's spatial profile on the single-shot measurement of its temporal profile," J. Opt. Soc. Am. B **25**(2008).

28. P. O'Shea, S. Akturk, M. Kimmel, and R. Trebino, "Practical issues in ultra-short-pulse measurements with 'GRENOUILLE'," Applied Physics B: Lasers and Optics **79**, 683-691 (2004).

29. D. Lee, Z. Wang, X. Gu, and R. Trebino, "Effect--and removal--of an ultrashort pulse's spatial profile on the single-shot measurement of its temporal profile," Journal of the Optical Society of America B **25**, A93-A100 (2008).

30. V. G. Dmitriev, G. G. Gurzadyan, and D. N. Nikogosyan, *Handbook of nonlinear optical crystals*, 3rd ed. (Springer-Verlag, Berlin, Germany, 1991).

31. X. Liu, R. Trebino, and A. V. Smith, "Numerical Simulations of the Ultrasimple Ultrashort-Laser-Pulse Measurement Technique, GRENOUILLE," in OSA Technical Digest Series (CD) (Optical Society of America, 2007), JThD8.

32. P. A. Jansson and M. Richardson, "Deconvolution of Images and Spectra, 2nd Edition," Optical Engineering **36**, 3224-3225 (1997).

33. S. Xiao and A. Weiner, "2-D wavelength demultiplexer with potential for > 1000 channels in the C-band," Opt. Express **12**, 2895-2902 (2004).

34. X. Shijun, A. M. Weiner, and C. Lin, "A dispersion law for virtually imaged phased-array spectral dispersers based on paraxial wave theory," Quantum Electronics, IEEE Journal of **40**, 420-426 (2004).

35. J. Cohen, P. Bowlan, V. Chauhan, and R. Trebino, "Measuring temporally complex ultrashort pulses using multiple-delay crossed-beam spectral interferometry," Opt. Express **18**, 6583-6597 (2010).

36. P. Bowlan, P. Gabolde, A. Shreenath, K. McGresham, and R. Trebino, "Crossed-beam spectral interferometry: a simple, high-spectral-resolution method for completely characterizing complex ultrashort pulses in real time," Optics Express **14**, 11892-11900 (2006).

37. B. Rubin and R. M. Herman, "Monochromators as light stretchers," Am. J. Phys. **49**, 868 (1981).

38. N. H. Schiller and R. R. Alfano, "Picosecond characteristics of a spectrograph measured by a streak camera/video readout system," Optics Communications **35**, 451-454 (1980).

39. P. Bowlan, P. Gabolde, M. A. Coughlan, R. Trebino, and R. J. Levis, "Measuring the spatiotemporal electric field of ultrashort pulses with high spatial and spectral resolution," Journal of the optical society of America B **25**, A81-A92 (2008).

40. J. P. Geindre, P. Audebert, S. Rebibo, and J. C. Gauthier, "Single-shot spectral interferometry with chirped pulses," Optics Letters **26**, 1612-1614 (2001).

41. C. Dorrer, M. Joffre, L. Jean-Pierre, and N. Belabas, "Spectral resolution and sampling issues in Fourier-transform spectral interferometry," Journal of the Optical Society of America B **17**, 1790-1802 (2000).

42. P. Bowlan, P. Gabolde, M. A. Coughlan, R. Trebino, and R. J. Levis, "Measuring the spatiotemporal electric field of ultrashort pulses with high spatial and spectral resolution," J. Opt. Soc. Am. B **25**, A81-A92 (2008).

43. P. Bowlan, P. Gabolde, and R. Trebino, "Directly measuring the spatio-temporal electric field of focusing ultrashort pulses," Optics Express **15**, 10219-10230 (2007).

44. A. S. Weling and D. H. Auston, "Novel sources and detectors for coherent tunable narrow-band terahertz radiation in free space," J. Opt. Soc. Am. B **13**, 2783-2791 (1996).

45. R. R. Alfano and S. L. Shapiro, "Observation of self-phase modulation and small-scale filaments in crystals and glasses," Physical Review Letters **24**, 592 (1970).

46. L. Lepetit, G. Chériaux, and M. Joffre, "Linear techniques of phase measurement by femtosecond spectral interferometry for applications in spectroscopy," J. Opt. Soc. Am. B **12**, 2467-2474 (1995).

47. P. O'Shea, M. Kimmel, X. Gu, and R. Trebino, "Highly simplified device for ultrashort-pulse measurement," Optics Letters **26**, 932-934 (2001).

48. K. Oba, P.-C. Sun, Y. T. Mazurenko, and Y. Fainman, "Femtosecond Single-Shot Correlation System: A Time-Domain Approach," Appl. Opt. **38**, 3810-3817 (1999).

49. R. Wyatt and E. Marinero, "Versatile single-shot background-free pulse duration measurement technique, for pulses of subnanosecond to picosecond duration," Applied Physics A: Materials Science & Processing **25**, 297-301 (1981).

50. P. Bowlan and R. Trebino, "Extreme pulse-front tilt from an etalon," J. Opt. Soc. Am. B *in press* (2010).

51. J. S. Lim, *Two-dimensional signal and image processing* (Prentice-Hall, Inc., 1990), pp. 469-476.

52. V. Chauhan, P. Bowlan, J. Cohen, and R. Trebino, "Single-diffraction-grating and grism pulse compressors," J. Opt. Soc. Am. B **27**, 619-624 (2010).